Article

# Simulations Show that Virus Assembly and Budding Are Facilitated by Membrane Microdomains

Teresa Ruiz-Herrero[1] and Michael F. Hagan[2,*]
[1]Departamento de Física Teórica de la Materia Condensada, Universidad Autónoma de Madrid, Madrid, España; and [2]Martin Fisher School of Physics, Brandeis University, Waltham, Massachusetts

ABSTRACT For many viruses, assembly and budding occur simultaneously during virion formation. Understanding the mechanisms underlying this process could promote biomedical efforts to block viral propagation and enable use of capsids in nanomaterials applications. To this end, we have performed molecular dynamics simulations on a coarse-grained model that describes virus assembly on a fluctuating lipid membrane. Our simulations show that the membrane can promote association of adsorbed subunits through dimensional reduction, but it also introduces thermodynamic and kinetic effects that can inhibit complete assembly. We find several mechanisms by which membrane microdomains, such as lipid rafts, reduce these effects, and thus, enhance assembly. We show how these predicted mechanisms can be experimentally tested. Furthermore, the simulations demonstrate that assembly and budding depend crucially on the system dynamics via multiple timescales related to membrane deformation, protein diffusion, association, and adsorption onto the membrane.

## INTRODUCTION

Processes in which proteins assemble on membranes to drive topology changes are ubiquitous in biology. Despite extensive experimental and theoretical investigations (e.g., Baumgart et al. (1) and Krauss and Haucke (2)), how assembly-driven membrane deformation depends on protein properties, membrane properties, and membrane compositional inhomogeneity, remains incompletely understood. An important example of this phenomenon occurs during the formation of an enveloped virus, when the virion acquires a membrane envelope by budding from its host cell. Budding is typically driven at least in part by assembly of capsid proteins or viral membrane proteins (3–8), and many enveloped viruses, including HIV and influenza, preferentially bud from membrane microdomains (e.g., lipid rafts) (5,9,10). Understanding how viruses exploit membrane domain structures to facilitate budding would reveal fundamental aspects of the viral lifecycle, and could focus efforts to identify targets for new antiviral drugs that interfere with budding.

There is much interest in developing enveloped viral nanoparticles as targeted transport vehicles equipped to cross cell membranes through fusion (11–13). More generally, identifying the factors that make viral budding robust will shed light on other biological processes in which high-order complexes assemble to reshape membranes. Toward this goal, we perform dynamical simulations in which capsids simultaneously assemble and bud from model lipid membranes. We identify mechanisms by which membrane adsorption either promotes or impedes assembly, and we find multiple mechanisms by which a membrane microdomain significantly enhances assembly and budding.

Enveloped viruses can be divided into two groups based on how they acquire their lipid membrane envelope. For the first group, which includes influenza and type C retroviruses (e.g., HIV), the (immature) nucleocapsid core assembles on the membrane concomitant with budding. In the second group, a core assembles in the cytoplasm before envelopment (reviewed in Sunquist and Kräusslich (3), Hurley et al. (4), and Welsch et al. (5)). In many families from this group, e.g., alphavirus, envelopment is driven by assembly of viral transmembrane glycoproteins around the core (14). For all enveloped viruses, membrane deformation is driven at least in part by a combination of weak protein-protein and protein-lipid interactions. Thus, properties of the membrane should substantially affect budding and assembly timescales. In support of this hypothesis, many viruses from both groups preferentially bud from membrane microdomains 10–100 nm in size that are concentrated with cholesterol and/or sphingolipids (5,9,10). A critical question is whether viruses utilize microdomains primarily to concentrate capsid proteins or other molecules, or if the geometric and physical properties of domains facilitate budding. Answering these questions through experiments alone has been challenging (3–5).

Extensive previous theoretical investigations have studied budding by preassembled cores or nanoparticles (e.g., Ruiz-Herrero et al. (15), Chaudhuri et al. (16), Deserno and Gelbart (17), Deserno and Bickel (18), Deserno (19), Fošnarič

*Submitted March 10, 2014, and accepted for publication December 5, 2014.*

*Correspondence: hagan@brandeis.edu

Teresa Ruiz-Herrero's present address is School of Engineering and Applied Sciences, Harvard University, Cambridge, Massachusetts.

Editor: Scott Feller.



0006-3495/15/02/0585/11 $2.00

http://dx.doi.org/10.1016/j.bpj.2014.12.017

et al. (20), Ginzburg and Balijepalli (21), Jiang et al. (22), Li and Xing (23), Li and Gu (24), Smith et al. (25), Tzlil et al. (26), Vácha et al. (27), Yang and Ma (28), and Dasgupta et al. (29,30)); or have budding triggered by nonassembling subunits (31); or have used continuum models to study assembly and budding (32,33). Most closely related to our work, Matthews and Likos (34–36) recently performed simulations on a coarse-grained model of patchy colloidal particles assembling on a membrane represented as a triangulated surface. These elegant simulations provided a first look at the process of simultaneous assembly and budding, and showed that subunit adsorption onto a membrane facilitates assembly through dimensional reduction. Here, we perform dynamical simulations on a model that more closely captures the geometric features of capsid subunits and lipid bilayers, and we explore how the presence of a microdomain within the membrane can influence assembly and budding.

Our simulations show that, while the membrane can promote assembly of partial capsids, free energy penalties and impeded diffusion of adsorbed subunits associated with membrane deformations can inhibit completion of assembly. We find that a microdomain within a certain size range favors membrane geometries that diminish these impediments, and thus can play a key role in enabling complete assembly and budding. Furthermore, our simulations suggest that assembly morphologies depend crucially on multiple timescales, including those of protein-protein association, membrane deformation, and protein adsorption onto the membrane. Finally, we discuss potential effects of simplifications in our coarse-grained model, and how a key prediction from the simulations can be tested in an in vitro assay.

## MATERIALS AND METHODS

Due to the large length- and timescales associated with assembly of a capsid, simulating the process with an all-atom model is beyond the capabilities of contemporary computers (37). Therefore, in this article we aim to elucidate the principles underlying simultaneous assembly and budding by considering a simplified geometric model for capsid proteins, inspired by previous simulations of empty capsid assembly (38–53) and assembly around nucleic acids (51,54–57). Similarly, we consider a simplified model for lipids (31,58) that recapitulates the material properties of biological membranes. Complete details of the model are provided in Supporting Materials and Methods in the Supporting Material; we summarize the model here.

### Membrane model

The membrane is represented by the model from Cooke and Deserno (58), in which each amphiphile is represented by one head bead and two tail beads connected by FENE bonds (Fig. 1 *c*). This is an implicit solvent model; hydrophobic forces responsible for the formation of bilayers are mimicked by attractive interactions between tail beads with interaction strength $\varepsilon_0$. This model enables computational feasibility while allowing the formation of bilayers with physical properties such as fluidity, diffusivity, and rigidity that are easily tuned across the range of values measured in biological membranes (15,58). The bead diameter is set to $\sigma = 0.9$ nm to obtain bilayers with widths of 5 nm and the lipid-lipid interaction strength is set to $k_BT/\varepsilon_0 = 1.1$ and $\omega_c = 1.5\sigma$ to obtain fluid membranes with bending modulus $\kappa = 8.25\ k_BT$.

When studying the effect of a domain, we consider two types of lipids, with *M* and *D* referring, respectively, to the lipids outside and inside of the domain, and tail-tail interaction parameters $\varepsilon_{ij}$ (see Eq. S6 in the Supporting Material) set to $\varepsilon_{DD} = \varepsilon_{MM} = \varepsilon_0$, while $\varepsilon_{DM}$ is a variable parameter that controls the domain line tension, $\gamma$. Varying $\varepsilon_{DM}$ from 0 to $\varepsilon_0$ tunes $\gamma$ from its maximum value to 0 (see The Membrane Model in the Supporting Material). Within the parameter range studied, the line tension can be approximated by $\gamma\sigma/k_BT \approx 22.9\text{–}24.7\varepsilon_{DM}/\varepsilon_0$ (see Fig. S3 in the Supporting Material).

### Capsid subunit model

We modified and extended a model for assembly of nonenveloped capsids (45,54,59,60) to describe assembly on a membrane. A complete listing of the interaction potentials is provided in The Capsid Subunit Model in the Supporting Material; we summarize them here. The capsid subunit is a rigid body with a pentagonal base and radius of $r_{pentamer} = 5\sigma$ formed by 15 attractive and 10 repulsive interaction sites (Fig. 1 *a* and see Fig. S4). Subunit assembly is mediated through a Morse potential between attractor pseudoatoms located in the pentagon plane, with one located at each subunit vertex and two along each edge. Attractions occur between like attractors only, meaning that there are vertex-vertex and edge-edge attractions, but no vertex-edge attractor interactions. The 10 repulsive interaction sites are arranged symmetrically above and below the pentagon plane, so as to favor a subunit-subunit angle consistent with a dodecahedron (116°). Further details are in The Capsid Subunit Model in the Supporting Material.

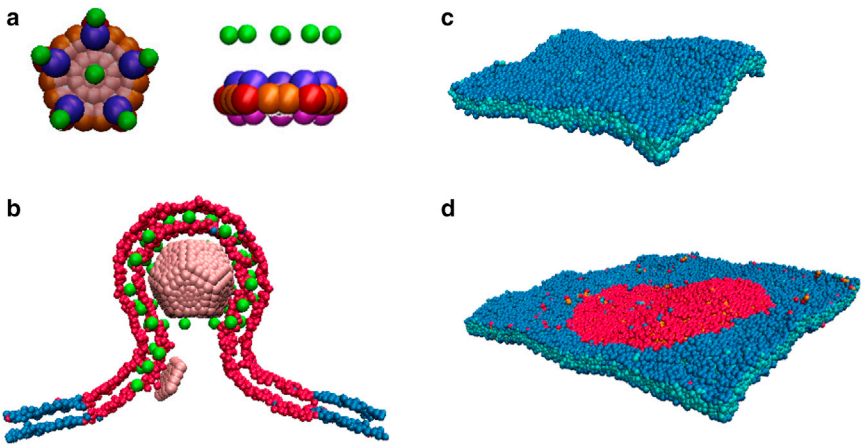


FIGURE 1 Capsomer and membrane models. (*A*) Top and side view of the capsomer. (*Red* and *orange*) Attractive sites; (*blue* and *purple*) top and bottom repulsive sites; (*pink*) excluders; and (*green*) capsomer-lipid interaction sites, with the pseudo-atom types defined in Methods and in The Capsid Subunit Model in the Supporting Material. (*B*) A slice of the membrane and the entire capsid are shown during budding. (*Green*) Capsomer-lipid interaction sites; (*red*) domain lipids. (*C*) Homogeneous membrane patch. (*Blue* and *cyan beads*) Lipid heads and lipid tails, respectively. (*D*) A two-phase membrane. (*Red* and *blue beads*) Domain and bulk lipid headgroups, respectively. To see this figure in color, go online.

## Membrane-capsomer interaction

The potential between capsomers and lipids accounts for attractive interactions and excluded-volume. We add to the capsomer body six attractor pseudoatoms that have attractive interactions with lipid tail beads. When simulating a phase-separated membrane, the attractors interact only with the domain lipid tails, except for simulations presented in Fig. S1. The attractors are placed one above each vertex and one above the center of the pentagon, each located a distance of $6\sigma$ above the pentagon plane (Fig. 1 *a*). These are motivated by, e.g., the myristate group on retrovirus GAG proteins that promotes subunit adsorption by inserting into the lipid bilayer (61). While in many cases the electrostatic interactions between capsid proteins and membrane polar headgroups also drive membrane adsorption, we did not explicitly include such an effect in order to reduce the number of model parameters. The attractor-tail interaction is the same form as the lipid tail-tail interaction except that there is no repulsive component (see Eq. S14 in the Supporting Material)). It is parameterized by the interaction strength, $\varepsilon_{ad}$, which tunes the adhesion free energy according to $e_{ad} = \alpha\varepsilon_{ad}$ with $\alpha = 2.276\sigma^{-2}$ (see Adhesion Energy in the Supporting Material).

To account for capsomer-lipid excluded-volume interactions, a layer of 35 excluder beads, each with diameter $1.25\sigma$, is placed in the pentagon plane (Fig. 1 *a*). Excluders experience repulsive interactions with all lipid beads. Because the mean location of the attractive interaction sites on adsorbed subunits is near the membrane midplane, the effective radius of the assembled capsid (not including the lipid coat) can be estimated from the distance between the attractors and the capsomer plane plus the capsid inradius (the radius of a sphere inscribed in a dodecahedron), which gives $R_{capsid} \approx 15.3\sigma$. As discussed below, this is smaller than any enveloped virus, and thus our results are qualitative.

In this work we are motivated by viruses such as HIV, where expression of the capsid protein (GAG) alone is sufficient for the formation of budded particles (62). Therefore, we consider a model that does not include viral transmembrane proteins (spike proteins). We also do not consider how some viruses use cellular machinery to drive scission (63), because this process is virus-specific and depends on detailed properties of cellular proteins. For those viruses our model may elucidate the mechanisms leading up to the point of scission.

## Simulations

Simulations were performed on GPUs with a modified version HOOMD 0.10.1 (64,65). We modified the Andersen barostat (66) implementation to simulate the membrane at constant temperature and constant frame tension (31) and to couple the barostat to rigid-body dynamics. The membrane was coupled to the thermostat and barostat with characteristic times $\tau_T = 0.4\tau_0$ and $\tau_P = 0.5\tau_0$, respectively, with $\tau_0$ the characteristic diffusion time for a lipid bead (defined below). The imposed frame tension was set to zero. Simulations with an alternative method to control tension (36) led to the same behavior.

Each capsomer was simulated as a rigid body using the Brownian dynamics algorithm, which uses the (non-overdamped) Langevin equation to evolve positions and rigid body orientations in time (64,65). To approximate the rotational dynamics of globular proteins, we modified the rigid-body algorithm in HOOMD so that forces and torques arising from drag and random buffeting were applied separately and isotropically. Finally, the code was modified to update rigid-body positions according to changes in the box size generated by the barostat at each time step.

Matthews and Likos (36) showed that hydrodynamic interactions (HI) between lipid particles can increase the rate of membrane deformation. However, since the mechanisms of assembly and budding appeared to be similar in simulations that did not include HI, the timescales for protein diffusion and association are only qualitative in a coarse-grained model, and the computational cost required to include HI is large in our more detailed model, we neglect HI in our simulations.

### Units

We set the units of energy, length, and time in our simulations equal to the characteristic energy, size, and diffusion time for a lipid bead of $\varepsilon_0$, $\sigma$, and $\tau_0$, respectively. The remaining parameters can be assigned physical values by setting the system to room temperature, $T = 300\ K$, and noting that the typical width of a lipid bilayer is ~5 nm, and the mass of a typical phospholipid is ~660 g/mol. The units of our system can then be assigned as follows:

$$\sigma = 0.9\ \text{nm},$$

$$m_0 = 220\ \text{g/mol},$$

$$\epsilon_0 = 3.77 \times 10^{-21} J = 227\ \text{g Å}^2/\text{ps}^2\text{mol}, \text{ and}$$

$$\tau_0 = \sigma\sqrt{m_0/\epsilon_0} = 8.86\ \text{ps}.$$

For each set of parameters, the results from four or more independent simulations were averaged to estimate the mean behavior of the system.

### Timescales

The diffusion coefficient of capsomers in solution is $D \approx 4.2\sigma^2/\tau_0$, while for capsomers adsorbed on the membrane, $D \in [0.004, 0.02]$ for $e_{ad}/\alpha k_B T$ ranging from 0.6 to 0.2. Thus timescales to diffuse by one capsomer diameter ($10\sigma$) are $\tau_d \approx 25\tau_0$ for capsomers in solution and $\tau_D \in [500, 2500]\tau_0$ on the membrane. We note that these timescales are qualitative, because the reduction in degrees of freedom associated with coarse-grained models reduces the ruggedness of the underlying free energy landscape (67). For example, comparison between the lipid model employed here with real values of lipid diffusion indicates a speed-up factor of ~$10^3$ (58).

### System

To simulate an infinite membrane, periodic boundary conditions were employed for the lateral dimensions and a wall was placed at the bottom of the box. Thus, the capsomers remained below the membrane unless they budded through it. To maintain a constant and equal ideal gas pressure above and below the membrane (despite the imbalance of capsomer concentrations), phantom particles were added to the system. These particles experienced excluded-volume interactions with the lipid head beads, and no other interactions.

For most simulations of inhomogeneous membranes the membrane contained $n = 16{,}200$ lipids, including those belonging to the domain. An initial bilayer configuration was equilibrated and then placed with its normal along the $z$ axis in a cubic box of side-length $L_x = L_y = 90\sigma$ and $L_z = 100\sigma$. For large domains ($r_{domain} > 40$) the membrane contained $n = 28{,}800$ lipids and the initial box size was $130 \times 130 \times 100\sigma^3$. For most simulations of homogeneous membranes, the bilayer contained $n = 7{,}164$ lipids and the initial box size was $63.5 \times 63.5 \times 100\sigma^3$; additional simulations on larger membranes were performed to rule out finite size effects.

The capsomers were introduced in the box in two different ways, to understand how the rate of subunit translation and/or targeting to the membrane affects assembly. The first set of simulations considered budding via quasi-equilibrium states, meaning that capsid proteins adsorb onto the membrane slowly in comparison to assembly and membrane deformation timescales. This scenario corresponds to the limit of low subunit concentration and a rate of subunit protein translation or targeting of subunits to the membrane, which is slow in comparison to assembly. Specifically, each capsomer was injected at ~$50\sigma$ below the membrane midplane once all previously injected subunits were part of the same cluster. For other simulations, capsomers were injected one by one with an interval $\tau_{inject}$ until reaching a predefined maximum number of subunits. In the limit of $\tau_{inject} = 0$, all capsomers were placed randomly at distances between

30 and 50$\sigma$ below the membrane at the beginning of the simulation. For all simulations, the initial configuration had three free capsomers placed at 30$\sigma$ below the membrane. Images were generated using the program VMD (68).

## RESULTS

To simulate capsid protein and membrane dynamics on time- and length-scales relevant to assembly and budding, we use the models illustrated in Fig. 1, *a* and *b*, and Fig. S4. The physical mechanisms that control the formation and size of domains (with a typical size of 10–100 nm) in cell membranes are poorly understood (69–71). To focus on the effect of a domain on assembly rather than its formation, we simulate a minimal heterogeneous membrane comprised of two lipid species, with interaction strengths that lead to phase separation within the membrane, with the minor species forming a circular domain (Fig. 1 *d*). The bulk membrane and domain have the same bending coefficient and area per lipid (to focus on mechanisms other than curvature- or bending stiffness-sorting (1)), but protein subunits preferentially partition into the domain (see Fig. S1; note that a complete listing of the interaction potentials is provided in Materials and Methods and see also The Capsid Subunit Model in the Supporting Material).

We performed simulations for a range of subunit-membrane interaction strengths $e_{ad}$, microdomain sizes $r_{domain}$, microdomain line tensions $\gamma$, and timescales for subunit association to the membrane $\tau_{inject}$. All simulations were performed with subunit-subunit interaction strengths of $\epsilon_{att}^{v} = 10.55\ k_BT$ and $\epsilon_{att}^{e} = 5.27\ k_BT$ between vertex and edge attractors respectively (see Supporting Materials and Methods in the Supporting Material). While assembly can proceed readily in bulk (into the same capsid geometry) under these conditions, in all simulations that we performed (for all values of $\tau_{inject}$) subunits adsorbed onto the membrane before assembling into any oligomer larger than a trimer. This behavior is consistent with enveloped viruses for which assembly in the cytosol is limited to small oligomers (e.g., HIV (72)). The results presented here correspond to long but finite simulation times, at which point assembly outcomes appeared roughly independent of increasing simulation time. Although these results need not necessarily correspond to equilibrium configurations, note that capsid assembly must proceed within finite timescales in in vivo or in vitro settings as well (73).

### The homogeneous membrane inhibits complete assembly

Given that capsid proteins may be targeted to the membrane rather than arriving by diffusion (74), we have considered several modes of introducing subunits into our simulated system, as described in Materials and Methods. We began by simulating assembly on a homogeneous membrane (a single species of lipid) (Fig. 1 *c*) via quasi-equilibrium states, meaning that free subunits were injected into the system far from the membrane one by one, each after all previously injected subunits were assembled (see Materials and Methods). This scenario corresponds to the limit of low subunit concentration and a rate of subunit protein translation or targeting of subunits to the membrane that is slow in comparison to assembly.

We found that assembly of membrane-absorbed subunits required large subunit-subunit interactions (as compared to those required for assembly in bulk solution), but that such subunits could undergo rapid nucleation on the membrane. However, we found no parameter sets for which our model undergoes complete assembly and budding on a homogeneous membrane. In most simulations, assembly slows dramatically after formation of a half-capsid (six subunits). The nature of subsequent assembly depends on the adhesion strength. For low adhesion strengths ($e_{ad} < 0.2\alpha$), assembly beyond a half-capsid occurs when particles detach from the membrane, sometimes leading to nearly completely assembled but partially wrapped capsids (Fig. 2, *a* and *b*). At intermediate adhesion strengths ($0.2 \leq e_{ad}/\alpha \leq 0.4$), particles do not readily dissociate from the membrane and assembly typically stalls at a half-capsid. Higher adhesion strengths ($e_{ad} > 0.4\alpha$) yield deformed, open structures that cannot drive complete budding (Fig. 2 *d*).

These results reveal that adsorption to a membrane has mixed effects on assembly. Through dimensional reduction,

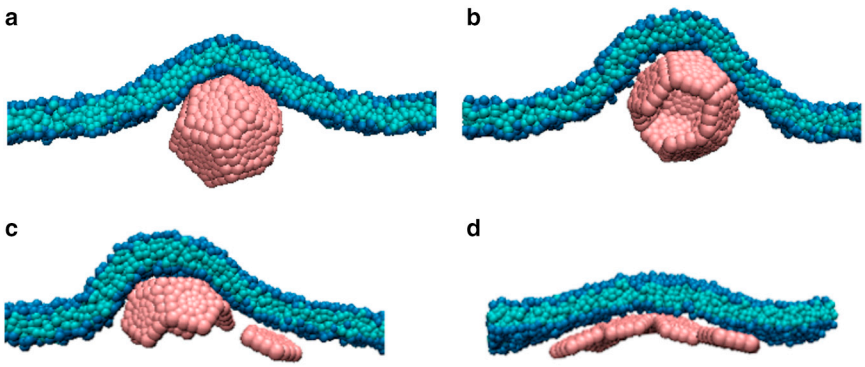


FIGURE 2 Typical end-products for assembly on a homogeneous membrane as a function of subunit-membrane adhesion strength $e_{ad}$. (*A* and *B*) Assembled but partially wrapped capsids for (*A*) $e_{ad} = 0.1\alpha$ and (*B*) $e_{ad} = 0.15\alpha$. (*C*) Assembly stalls at a half capsid for $e_{ad} = 0.2\alpha$. (*D*) A deformed, open structure forms for $e_{ad} = 0.4\alpha$. To see this figure in color, go online.

membrane adsorption reduces the search space and can reduce nucleation barriers by generating a high local subunit concentration (34,36). Similar effects occur during assembly on a polymer (54–56,73,75,76). However, assembly on the membrane also introduces new impediments to assembly.

Formation of a completely enveloped capsid incurs a membrane bending free energy cost of $8\pi\kappa$, independent of capsid size (77). This free energy penalty must be compensated by subunit-subunit and subunit-membrane interactions. In our model the subunit-membrane interactions do not promote membrane curvature, and thus large subunit-subunit interactions are required for assembly on the membrane. For these parameters, nucleation also occurs in bulk solution if there is no membrane present (nucleation did not occur in bulk solution with a membrane present for any value of $\tau_{\text{inject}}$ because subunits adsorbed onto the membrane before undergoing nucleation). We also considered a model in which the surface of the subunit is curved (see Fig. S10), so that subunit-membrane adsorption does promote local curvature. Interestingly, this model did not lead to improved assembly as compared to the flat subunits.

This result and the frustrated assembly dynamics of half-capsid intermediates illustrate the fact that the geometry and energetics of membranes affect the assembly of membrane-associated proteins in multiple ways, altering both the probability of binding for subunits in the vicinity of an assemblage and the apparent diffusion-limited flux of subunits to the assemblage. Once intermediates reach one-half the capsid size, additional subunits approach with orientations that are not conducive to association. Addition of such a subunit requires a large membrane deformation, which is energetically unfavorable for physically relevant values of the membrane bending rigidity and thus rare (see Fig. S6 *b*). Assembly therefore stalls or, in the case of weak adhesion energy, proceeds by detachment of subunits from the membrane leading to assembled but partially wrapped capsids. The stalled assembly states resemble the partially assembled states predicted theoretically (32,33), while the partially wrapped capsids are consistent with the metastable partially wrapped states found for a preassembled particle in our previous simulations (15). A second impediment to assembly arises because subunit-membrane attractions are reduced in regions where the membrane curvature is large on the length scale of the rigid subunit (see Fig. S7). This effect hinders subunit diffusion across the neck (see Movies S1 and S2), therefore decreasing the flux of subunits to the assembling capsid.

As discussed below, the large magnitude of the membrane-induced barrier to assembly arises in part due to the small capsid size and relatively large subunits of our model. However, the barrier is intrinsic to assembly of a spherical or convex polygonal structure on a deformable two-dimensional manifold, and thus will exist for any such model.

## Assembly and budding from a membrane microdomain

We next simulated assembly in the presence of a phase-separated membrane (Fig. 1 *d*) to understand the effects of a membrane domain on assembly and budding. While the mechanisms by which rafts form are incompletely understood, we focus on the effect that the presence of a domain can exert on assembly and budding. We emphasize that we consider lipid-lipid interaction parameters and domain sizes for which the domain is flat and stable in the absence of capsid subunits (see Fig. S3 *b*); i.e., the domain line tension is insufficient to drive budding. We first consider budding in the quasi-equilibrium limit.

### *Effect of line tension and adhesion energy*

Fig. 3 (*left*) shows the predominant final system configurations as a function of $e_{\text{ad}}$ and line tension for fixed domain size $r_{\text{domain}} = 35\sigma$, which corresponds to 1.3 times the area required to wrap the capsid. Moderate adhesion strengths and small line tensions lead to complete assembly and budding (Fig. 4), meaning that: 12 subunits form a complete capsid, the capsid is completely wrapped by the membrane, and the membrane undergoes scission through spontaneous fusion of the neck to release the membrane-enveloped capsid. Because it requires a relatively large thermal fluctuation, scission is characterized by long timescales. After scission, the portion of the domain not enveloping the capsid remains within the membrane.

Analysis of simulation trajectories identified three mechanisms by which the domain facilitates assembly. First, partitioning of adsorbed proteins into the domain generates a high local subunit concentration, and thus, promotes nucleation. However, in simulations in which the degree of subunit partitioning into the domain was varied (see Fig. S1), the outcome was insensitive to this parameter. This insensitivity arises because our system requires strong subunit-subunit interactions to drive membrane bending and thus nucleation occurs readily. Second, as noted in the case of spherical particle budding through a raft (25), the domain line tension promotes membrane curvature (buckling), because buckling reduces the length of the domain interface (78). While a positive membrane tension inhibits budding (19), the effective compressive force arising due to line tension promotes budding. Modeling the partial capsid as a hemispherical cap (79), and neglecting curvature outside the vicinity of the capsid (see Theoretical Analysis on the Effect of the Domain on Neck Geometry in the Supporting Material, and Foret (33)), the length of the interface as a function of number of subunits $n$ in a partial capsid is given by

$$l_{\text{int}}(n, r_{\text{domain}}) = 2\pi\left[r_{\text{domain}}^2 - \left(2R_{\text{capsid}}n/N\right)^2\right]^{1/2}, \quad (1)$$

with $N = 12$ the number of subunits in a capsid and $R_{\text{capsid}} \approx 15.3\sigma$ as the capsid radius. The change in

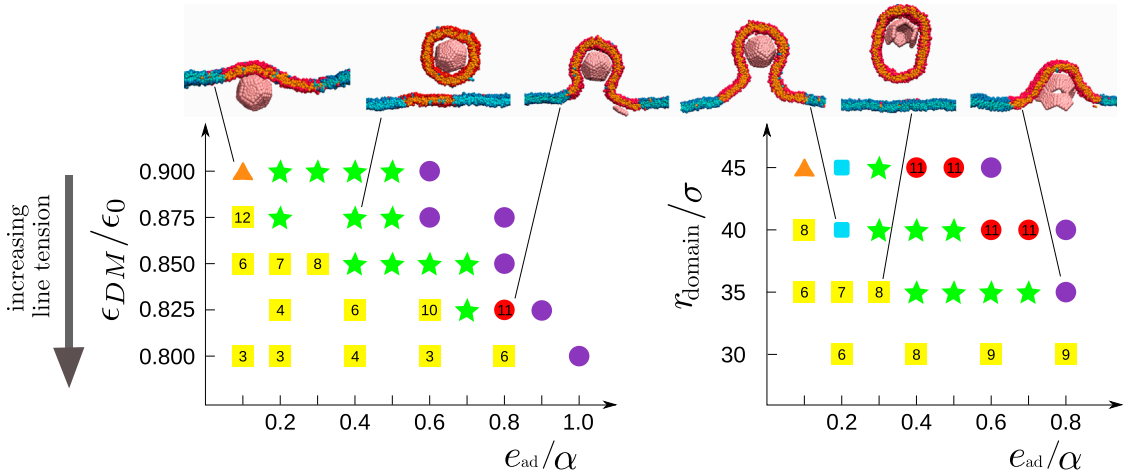


FIGURE 3 Predominant end-products from assembly simulations via quasi-equilibrium states with a membrane microdomain, as a function of adhesion strength $e_{ad}$ and (*left*) line tension ($\gamma\sigma/k_BT \approx 22.9$–$24.7\epsilon_{DM}/\epsilon_0$) with fixed domain radius $r_{domain} = 35\sigma$ and (*right*) varying $r_{domain}$ with fixed line tension $\epsilon_{DM}/\epsilon_0 = 0.85$ ($\gamma \approx 1.9\ k_BT/\sigma$) and $\alpha = 2.276\sigma^{-2}$. The most frequent outcomes are indicated as complete assembly and budding (*green solid stars*); budding of the entire domain before assembly completes, with the number indicating the typical partial capsid size upon budding (*yellow solid squares*); complete assembly but incomplete wrapping (*orange solid triangles*); stalled assembly with wrapping (*red solid circles*); complete assembly and wrapping without fusion of the neck (*blue squares*); and malformed assembly (*purple circles*). Snapshots from simulations for the corresponding parameter sets are also shown. The complete distribution of outcome frequencies and assembly times are shown for some parameter sets in Fig. S11 and Fig. S12. To see this figure in color, go online.

interfacial energy between a flat domain and a completely wrapped capsid is then given by

$$\Delta E_{int}/k_BT = 2\pi\gamma r_{domain}\left[1 - \left(1 - 4R_{capsid}^2/r_{domain}^2\right)^{1/2}\right]. \quad (2)$$

For $r_{domain} = 35\sigma$ and $\gamma = 1.9\ k_BT/\sigma$, we have $\Delta E_{int} \approx -215\ k_BT$, which is comparable to the total bending energy associated with a wrapped capsid, $E_{bend} = 8\pi\kappa = 207\ k_BT$. The significance of this effect and consequently the ability of a domain to promote budding diminishes as the domain size becomes large in comparison to the capsid (see Fig. S2).

The simulations also identified a third effect of the domain that promotes complete assembly—the presence of the domain interface changes the geometry of the membrane in the vicinity of the capsid intermediate, promoting a long shallow neck. While curvature energy favors capsid assembly in the domain interior, the line tension is minimized by a neck that extends to the domain interface. The relatively

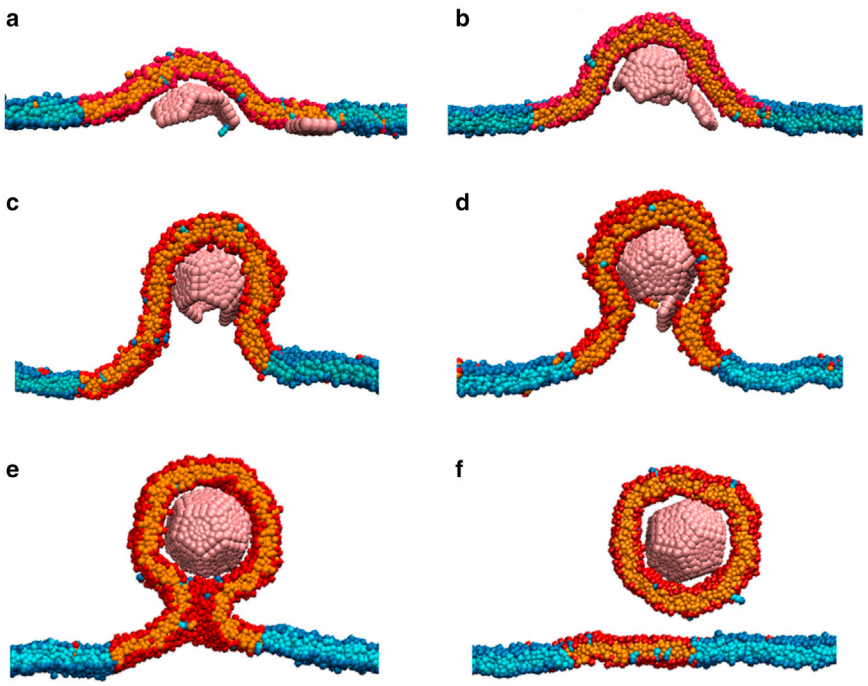


FIGURE 4 Capsid assembly and budding from a domain. Two-dimensional slices of configurations at different times extracted from MD simulations for $e_{ad} = 0.4\alpha$, $r_{domain} = 35\sigma$, and $\epsilon_{DM}/\epsilon_0 = 0.875$ ($\gamma \approx 1.3\ k_BT/\sigma$). The membrane wraps the growing capsid (*A–D*) until the complete, enveloped capsid is connected to the rest of the membrane by a narrow neck (*E*). Finally, thermal fluctuations lead to fusion of the neck and the encapsulated capsid escapes from the membrane (*F*). To see this figure in color, go online.

shallow curvature of such a neck reduces the impediments to assembly on a membrane discussed in the previous section. Subunits diffuse readily across a long neck, and subsequent attachment to the assembling capsid incurs relatively small membrane deformation energies. The influence of the neck in subunit diffusion and association is illustrated by animations from assembly trajectories in Movie S1 and Movie S2. Formation of a long neck is governed by a competition between the loss of subunit-membrane adhesion energy associated with partial detachment from the capsid and the reduction in interfacial energy caused by the extended neck. The free energy difference between tightly wrapped capsids and extended necks is approximately calculated in Fig. S9, which indicates that moderate adhesion energies and small domains favor extended necks.

Outside of optimal parameter values, we observe five classes of alternative end-products, as follows:

1. For large values of $\gamma$ or small domains, formation of a partial capsid triggers budding of the entire domain before assembly completes. Budding of the whole domain is driven by the interfacial energy, $E_{\mathrm{int}}(n,r_{\mathrm{domain}}) = \gamma l_{\mathrm{int}}(n,r_{\mathrm{domain}})$. In the absence of assembly ($n = 0$), this driving force is insufficient to overcome the deformation free energy barrier to domain budding for the parameters we simulate. However, assembly of a partial capsid intermediate stabilizes curvature and thus reduces the bending energy required for budding of the whole domain. A simple estimate of this effect is obtained by assuming that the partial capsid compensates for the bending energy of a budded domain by an amount proportional to its wrapped area:

$$E_{\mathrm{bend}}(n, r_{\mathrm{domain}}) = 8\pi\kappa\left[1 - 4\left(R_{\mathrm{capsid}}/r_{\mathrm{domain}}\right)^2(n/N)\right]. \quad (3)$$

Following Lipowsky (78), budding of the whole domain is favorable when $E_{\mathrm{int}}(n,r_{\mathrm{domain}}) > E_{\mathrm{bend}}(n,r_{\mathrm{domain}})$. However, larger intermediates are required for budding to be spontaneous, thus enabling assembly to complete. Furthermore, for $r_{\mathrm{domain}} > 2R_{\mathrm{capsid}}$ and intermediates beyond a half-capsid ($n > N/2$), wrapping of the intermediate produces curvature incommensurate with whole-domain budding. Higher values of $e_{\mathrm{ad}}$ promote tight wrapping with strong curvature of the capsid, and thus disfavor whole-domain budding (Fig. 4 *B*).

2. For small $\gamma$ and $e_{\mathrm{ad}}$, the capsid assembles but wrapping is incomplete. Here the subunit-membrane adhesion energy is insufficient to compensate for the membrane bending energy cost associated with wrapping.
3. For larger-than-optimal adhesion strengths, the membrane wraps the assembling capsid tightly with a short neck. As discussed in the previous section, the high curvature associated with a short neck inhibits association of the final subunit leading to stalled, incomplete assembly.
4. For large $e_{\mathrm{ad}}$, subunit-membrane adhesion energy dominates over subunit-subunit interactions leading to misassembled structures.
5. At other domain sizes (Fig. 4, *right*) we observe configurations in which the capsid is completely wrapped, but the neck does not undergo scission. To illustrate the timescales, interactions, and coupling between assembly and membrane configurations, the total subunit-subunit attractive interaction energy and the magnitude of membrane deformation are plotted as a function of time for a trajectory leading to each type of outcome in Fig. 5.

### *Effect of domain size*

The dependence of assembly and budding on the domain radius $r_{\mathrm{domain}}$ for constant line tension $\gamma = 1.9\, k_{\mathrm{B}}T/\sigma$ is shown in Fig. 3 (*right*). There is an optimal domain size ~1–2 times the area of a wrapped capsid ($35\sigma \lesssim r_{\mathrm{domain}} \lesssim 40\sigma$) that leads to robust assembly and budding over a broad range of adhesion energies $e_{\mathrm{ad}}$. For smaller domains, low values of adhesion lead to budding of the entire domain before assembly completes. In the absence of protein assembly, line tension triggers budding above a threshold domain size; smaller domains are stable because bending energy dominates over interfacial energy (78). However, we find here that partial capsid intermediates stabilize membrane deformation over an area proportional to their size, and thus drive budding within domains below a threshold

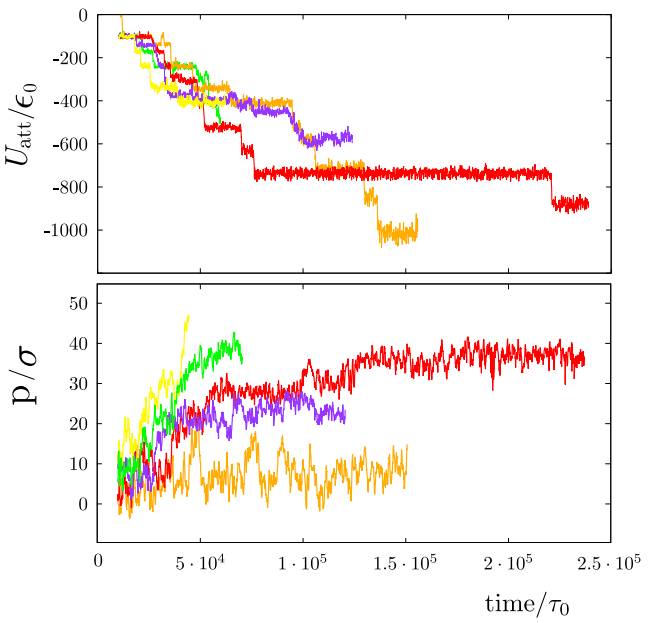


FIGURE 5 Total subunit-subunit attractive interaction energy *(top)* and amplitude of membrane deformation, measured by the capsid penetration, $p$ *(bottom)*, as a function of time for a trajectory leading to each type of outcome described in the main text. The capsid penetration $p$ is measured as the distance between the top of the capsid and the center of mass of the membrane. The color code represents the outcome type and follows the same format as in Fig. 3: successful assembly (*green*), budding of a partial capsid (*yellow*), complete assembly but incomplete wrapping (*orange*), stalled assembly with wrapping (*red*) and malformed assembly (*violet*). To see this figure in color, go online.

size (Eq. 3). On the other hand, for larger-than-optimal domains the assembling capsid only deforms a fraction of the domain; thus, the domain interface does not promote a long neck (see Fig. S9), and it provides a smaller driving force due to interfacial energy (Eq. 3). The behavior of such domains is therefore comparable to that in a homogeneous membrane.

### *Effect of subunit adsorption timescale*

In the quasi-equilibrium simulations discussed so far, the assembly outcomes were determined by the relative timescales of membrane deformation and partial capsid annealing. To determine the effect of the subunit adsorption timescale, we characterized the system behavior for subunit injection timescales $\tau_{\text{eject}}$ (see Materials and Methods) between the quasi-equilibrium limit and 0, where all subunits were introduced at the inception of the simulation (Fig. 6). We set $r_{\text{domain}} = 35\sigma$.

The predominant end-products are shown as a function of the adhesion strength and the subunit injection timescale in Fig. 6. We see that the qualitative behavior is independent of the injection timescale; for all injection rates there is range of intermediate adhesion strengths at $\sim e_{\text{ad}} = 0.4\alpha$, for which complete assembly and budding is observed. However, as the injection timescale decreases, both the lower and upper bounds of this optimal range shift to weaker adhesion energies. Weak adhesion energies avoid malformed assemblages and also increase the timescale for budding of the entire domain (because domain curvature is less stabilized), thus increasing the probability of complete well-formed capsids. However, overly weak adhesion energies lead to longer necks (see Fig. S9) that reduce the timescale for budding of the entire domain, so that, even at high injection rates, budding precedes capsid completion. Stronger-than-optimal adhesion energies tend to result in malformed assemblages (see Fig. S13 *b*) at the lower injection timescales.

This result can be understood from previous studies of assembly into empty capsids or around polymers (39,41,51,55,73,80,81)—higher adhesion energies lead to an exponential increase in the timescale for annealing of partial capsid configurations; kinetic traps occur when annealing timescales exceed the subunit binding timescale. The ultimate fate of these large aggregates depends on the adhesion energy $e_{\text{ad}}$. For smaller-than-optimal adhesion energies, assemblages are loosely wrapped and the entire domain undergoes budding once the assemblage reaches a threshold size (e.g., Fig. S13 *b*). For larger $e_{\text{ad}}$, malformed aggregates are tightly wrapped by the membrane and remain attached by a neck (e.g., Fig. S13 *a*). The shortest injection timescales and largest adhesion energies we investigated lead to large flat aggregates that do not bend the membrane (see Fig. S13 *c*), or partial capsids emerging from a flat aggregate (see Fig. S13 *d*). Finally, we note that as the subunit injection timescale is decreased, the diversity of outcomes at a given parameter set increases and thus the yield of budded, well-formed capsids decreases (see Fig. S15).

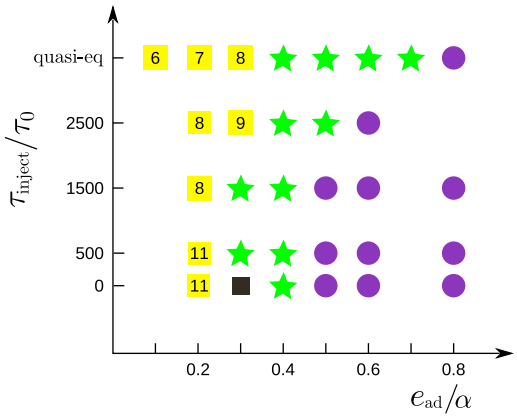


FIGURE 6 Predominant end-products as a function of the subunit injection timescale $\tau_{\text{inject}}$ and the adhesion strength $e_{\text{ad}}$ are shown for a domain with $r_{\text{domain}} = 25\sigma$ and $\gamma = 1.9\ k_{\text{B}}T/\sigma$. The most frequent outcome is shown for every set of parameters. (Symbols are defined as in Fig. 3 except for *black solid square symbols*, which denote budding of the whole domain with a malformed capsid inside.) Alternative outcomes observed at some parameter sets are documented in Fig. S15. To see this figure in color, go online.

### *Effect of subunit copy number*

We found that the dynamics is qualitatively similar when excess subunits are included in the simulation. For example, we performed simulations on systems with 19 capsomers, ~60% more than needed for capsid formation. For an injection timescale of $\tau_{\text{eject}} = 500\tau_0$, the behavior is similar to the small $\tau_{\text{eject}}$ results discussed above, except that subunits on the periphery of an assembling capsid typically form flat aggregates that can hinder budding (see Fig. S14). For adhesion strengths between 0.3 and 0.4 $\varepsilon_0$, budding is observed (see Fig. S14), whereas larger values of $e_{\text{ad}}$ lead to the forms of kinetic traps discussed above.

## DISCUSSION

Our simulations demonstrate that, while a fluctuating membrane can promote assembly through dimensional reduction, it also can inhibit complete assembly by limiting the orientational fluctuations and diffusion of adsorbed subunits. These effects, which are not present for assembly in bulk solution (73), can engender metastable partially assembled or partially budded structures. While the degree of inhibition may depend on the specific membrane and protein properties (see below), it is generic to the assembly of a curved structure on a deformable surface. We find that assembly from a membrane microdomain can substantially diminish these effects, which could partly account for the prevalence of enveloped viruses that preferentially bud from lipid rafts or other membrane microdomains.

As an initial exploration of the relationship between membrane domain structure and budding, we considered a

minimal model for a microdomain, which accounts only for preferential partitioning or targeting of capsid proteins within the domain. Our simulations identified three effects by which such a domain can promote assembly and budding.

1. Generating a high local concentration of adsorbed subunits,
2. Generating a buckling pressure that promotes budding, and
3. Enhancing the diffusive flux of subunits to the assembling capsid by lengthening the neck around the budding capsid.

Importantly, the predicted effects are sensitive to the domain size (Fig. 3), with an optimal domain size of ~1–2 times the area of a wrapped capsid. Smaller domains lead to budding before completion of assembly, whereas facilitation of budding becomes ineffective when the domain radius becomes large in comparison to the capsid size. These predictions could be tested by in vitro experiments in which capsid proteins assemble and bud from multicomponent artificial phospholipid vesicles as studied for other membrane-associated proteins (e.g., Becalska et al. (82), Thiam et al. (83), and Manneville et al. (84)) with phase-separated or heterogeneous vesicles (e.g., Manneville et al. (84)).

Finally, we consider the limitations of the model studied here. The effective diameter of our enveloped $T = 1$ capsid is ~28 nm, while the smallest enveloped viruses found in nature have diameters of 40–50 nm (e.g., Jones et al. (85)). Although the relationship between particle size and budding has been explored in detail for preassembled nucleocapsids or nanoparticles (e.g., Ruiz-Herrero et al. (15), Ginzburg and Balijepalli (21), and Yue and Zhang (86)), to our knowledge, our simulations here have identified new factors that control simultaneous assembly and budding. During assembly of a larger capsid, each subunit would individually comprise a smaller fraction of the total capsid area and thus would incur a smaller increment of membrane deformation energy when associating with the capsid. Similarly, intrasubunit degrees of freedom could allow subunit distortions that would facilitate diffusion across the neck. However, note that such distortions would themselves involve free energy penalties and thus would still hinder diffusion.

In principle, other forms of excluded-volume interaction with the membrane could improve subunit diffusion, but changing the softness of the repulsive excluded volume interaction between our subunits in the membrane did not change the results. We also note that the potential used for the subunit-membrane interaction in this work does not represent local distortions of the lipid hydrophobic tails resulting from insertion of a hydrophobic group. Such insertions could lead to local membrane curvatures and membrane-mediated subunit interactions that could either facilitate or hinder assembly and budding; the study of these phenomena is an open and active field (e.g., Weikl et al. (87), Semrau et al. (88), Reynwar and Deserno (89), Goulian et al. (90), and Deserno (67)). Given the qualitative nature of subunit-subunit interactions in our model, we do not expect these effects to qualitatively change the results.

To minimize the number of model parameters, we have set the material constants (e.g., bending modulus and fluidity) equal for the domain and background lipid species. Although this study demonstrates three contributions by which such a domain can promote membrane deformation, it will be interesting to explore additional effects that may arise due to varying material properties within microdomains (1). For example, it is believed that biological rafts have higher bending moduli than nonraft membrane environments. Similarly, for some viruses important roles are played by recruitment of additional viral proteins (6), other cellular factors that create or support membrane curvature (4,91,92), and cytoskeletal machinery that actively drives budding (e.g., Welsch et al. (5), Balasubramaniam and Freed (74), Taylor et al. (93), and Gladnikoff et al. (94)).

While these results can be systematically incorporated into the model, our simulations provide a starting point to understand how microdomains facilitate budding and, through comparison with experiments, to identify the critical steps in budding.

## SUPPORTING MATERIAL

Supporting Materials and Methods, fifteen figures, and two movies are available at http://www.biophysj.org/biophysj/supplemental/S0006-3495(14)04762-6.

## ACKNOWLEDGMENTS

Computational resources were provided by the National Science Foundation through XSEDE computing resources (Longhorn, Keeneland, and Maverick) and the Brandeis HPCC, which is partially supported by the Brandeis University NSF MRSEC DMR-1420382 (see below).

This work was supported by award No. R01GM108021 from the National Institute of General Medical Sciencesthe Brandeis University NSF MRSEC DMR-1420382, MODELICO grant No. S2009/ESP-1691 from Comunidad Autónoma de Madrid, and grant No. FIS2010-22047-C05-01 from Ministerio de Ciencia e Innovación de España.

## SUPPORTING CITATIONS

References (95–99) appear in the Supporting Material.

## REFERENCES

1. Baumgart, T., B. R. Capraro, …, S. L. Das. 2011. Thermodynamics and mechanics of membrane curvature generation and sensing by proteins and lipids. *Annu. Rev. Phys. Chem.* 62:483–506.
2. Krauss, M., and V. Haucke. 2011. Shaping membranes for endocytosis. *In* Reviews of Physiology, Biochemistry and Pharmacology, *Vol. 161*. S. G. Amara, E. Bamberg, B. K. Fleischmann, T. Gudermann, R. Jahn, W. J. Lederer, R. Lill, B. Nilius, and S. Offermanns, editors. Springer, Berlin, Germany, pp. 45–66.

3. Sundquist, W. I., and H.-G. Kräusslich. 2012. HIV-1 assembly, budding, and maturation. *Cold Spring Harb. Perspect. Med.* 2:a006924.
4. Hurley, J. H., E. Boura, …, B. Różycki. 2010. Membrane budding. *Cell.* 143:875–887.
5. Welsch, S., B. Müller, and H.-G. Kräusslich. 2007. More than one door—budding of enveloped viruses through cellular membranes. *FEBS Lett.* 581:2089–2097.
6. Solon, J., O. Gareil, …, Y. Gaudin. 2005. Membrane deformations induced by the matrix protein of vesicular stomatitis virus in a minimal system. *J. Gen. Virol.* 86:3357–3363.
7. Vennema, H., G. J. Godeke, …, P. J. Rottier. 1996. Nucleocapsid-independent assembly of coronavirus-like particles by co-expression of viral envelope protein genes. *EMBO J.* 15:2020–2028.
8. Garoff, H., R. Hewson, and D.-J. E. Opstelten. 1998. Virus maturation by budding. *Microbiol. Mol. Biol. Rev.* 62:1171–1190.
9. Waheed, A. A., and E. O. Freed. 2010. The role of lipids in retrovirus replication. *Viruses.* 2:1146–1180.
10. Rossman, J. S., and R. A. Lamb. 2011. Influenza virus assembly and budding. *Virology.* 411:229–236.
11. Lundstrom, K. 2009. Alphaviruses in gene therapy. *Viruses.* 1:13–25.
12. Cheng, F., I. B. Tsvetkova, …, S. Mukhopadhyay. 2013. The packaging of different cargo into enveloped viral nanoparticles. *Mol. Pharm.* 10:51–58.
13. Rowan, K. 2010. Oncolytic viruses move forward in clinical trials. *J. Natl. Cancer Inst.* 102:590–595.
14. Garoff, H., M. Sjöberg, and R. H. Cheng. 2004. Budding of alphaviruses. *Virus Res.* 106:103–116.
15. Ruiz-Herrero, T., E. Velasco, and M. F. Hagan. 2012. Mechanisms of budding of nanoscale particles through lipid bilayers. *J. Phys. Chem. B.* 116:9595–9603.
16. Chaudhuri, A., G. Battaglia, and R. Golestanian. 2011. The effect of interactions on the cellular uptake of nanoparticles. *Phys. Biol.* 8:04600.
17. Deserno, M., and W. M. Gelbart. 2002. Adhesion and wrapping in colloid-vesicle complexes. *J. Phys. Chem. B.* 106:5543–5552.
18. Deserno, M., and T. Bickel. 2003. Wrapping of a spherical colloid by a fluid membrane. *Europhys. Lett.* 62:767.
19. Deserno, M. 2004. Elastic deformation of a fluid membrane upon colloid binding. *Phys. Rev. E Stat. Nonlin. Soft Matter Phys.* 69: 031903.
20. Fošnarič, M., A. Iglič, …, S. May. 2009. Monte Carlo simulations of complex formation between a mixed fluid vesicle and a charged colloid. *J. Chem. Phys.* 131:105103.
21. Ginzburg, V. V., and S. Balijepalli. 2007. Modeling the thermodynamics of the interaction of nanoparticles with cell membranes. *Nano Lett.* 7:3716–3722.
22. Jiang, W., B. Y. S. Kim, …, W. C. W. Chan. 2008. Nanoparticle-mediated cellular response is size-dependent. *Nat. Nanotechnol.* 3:145–150.
23. Li, X., and D. Xing. 2010. A simple method to evaluate the optimal size of nanoparticles for endocytosis based on kinetic diffusion of receptors. *Appl. Phys. Lett.* 97:153704.
24. Li, Y., and N. Gu. 2010. Thermodynamics of charged nanoparticle adsorption on charge-neutral membranes: a simulation study. *J. Phys. Chem. B.* 114:2749–2754.
25. Smith, K. A., D. Jasnow, and A. C. Balazs. 2007. Designing synthetic vesicles that engulf nanoscopic particles. *J. Chem. Phys.* 127:084703.
26. Tzlil, S., M. Deserno, …, A. Ben-Shaul. 2004. A statistical-thermodynamic model of viral budding. *Biophys. J.* 86:2037–2048.
27. Vácha, R., F. J. Martinez-Veracoechea, and D. Frenkel. 2011. Receptor-mediated endocytosis of nanoparticles of various shapes. *Nano Lett.* 11:5391–5395.
28. Yang, K., and Y.-q. Ma. 2011. Wrapping and internalization of nanoparticles by lipid bilayers: a computer simulation study. *Aust. J. Chem.* 64:894.
29. Dasgupta, S., T. Auth, and G. Gompper. 2014. Shape and orientation matter for the cellular uptake of nonspherical particles. *Nano Lett.* 14:687–693.
30. Dasgupta, S., T. Auth, and G. Gompper. 2013. Wrapping of ellipsoidal nano-particles by fluid membranes. *Soft Matter.* 9:5473–5482.
31. Reynwar, B. J., G. Illya, …, M. Deserno. 2007. Aggregation and vesiculation of membrane proteins by curvature-mediated interactions. *Nature.* 447:461–464.
32. Zhang, R., and T. T. Nguyen. 2008. Model of human immunodeficiency virus budding and self-assembly: role of the cell membrane. *Phys. Rev. E Stat. Nonlin. Soft Matter Phys.* 78:051903.
33. Foret, L. 2014. Shape and energy of a membrane bud induced by protein coats or viral protein assembly. *Eur. Phys. J. E Soft Matter.* 37:42.
34. Matthews, R., and C. Likos. 2012. Influence of fluctuating membranes on self-assembly of patchy colloids. *Phys. Rev. Lett.* 109:178302.
35. Matthews, R., and C. N. Likos. 2013. Structures and pathways for clathrin self-assembly in the bulk and on membranes. *Soft Matter.* 9:5794–5806.
36. Matthews, R., and C. N. Likos. 2013. Dynamics of self-assembly of model viral capsids in the presence of a fluctuating membrane. *J. Phys. Chem. B.* 117:8283–8292.
37. Freddolino, P. L., A. S. Arkhipov, …, K. Schulten. 2006. Molecular dynamics simulations of the complete satellite tobacco mosaic virus. *Structure.* 14:437–449.
38. Schwartz, R., P. W. Shor, …, B. Berger. 1998. Local rules simulation of the kinetics of virus capsid self-assembly. *Biophys. J.* 75:2626–2636.
39. Hagan, M. F., and D. Chandler. 2006. Dynamic pathways for viral capsid assembly. *Biophys. J.* 91:42–54.
40. Hicks, S. D., and C. L. Henley. 2006. Irreversible growth model for virus capsid assembly. *Phys. Rev. E Stat. Nonlin. Soft Matter Phys.* 74:031912.
41. Nguyen, H. D., V. S. Reddy, and C. L. Brooks, 3rd. 2007. Deciphering the kinetic mechanism of spontaneous self-assembly of icosahedral capsids. *Nano Lett.* 7:338–344.
42. Wilber, A. W., J. P. K. Doye, …, P. Wong. 2007. Reversible self-assembly of patchy particles into monodisperse icosahedral clusters. *J. Chem. Phys.* 127:085106.
43. Nguyen, H. D., and C. L. Brooks, 3rd. 2008. Generalized structural polymorphism in self-assembled viral particles. *Nano Lett.* 8:4574–4581.
44. Nguyen, H. D., V. S. Reddy, and C. L. Brooks, 3rd. 2009. Invariant polymorphism in virus capsid assembly. *J. Am. Chem. Soc.* 131: 2606–2614.
45. Johnston, I. G., A. A. Louis, and J. P. K. Doye. 2010. Modelling the self-assembly of virus capsids. *J. Phys. Condens. Matter.* 22:104101.
46. Wilber, A. W., J. P. K. Doye, …, A. C. F. Lewis. 2009. Monodisperse self-assembly in a model with protein-like interactions. *J. Chem. Phys.* 131:175102.
47. Wilber, A. W., J. P. K. Doye, and A. A. Louis. 2009. Self-assembly of monodisperse clusters: dependence on target geometry. *J. Chem. Phys.* 131:175101.
48. Rapaport, D., J. Johnson, and J. Skolnick. 1999. Supramolecular self-assembly: molecular dynamics modeling of polyhedral shell formation. *Comput. Phys. Commun.* 121–122:231–235.
49. Rapaport, D. C. 2004. Self-assembly of polyhedral shells: a molecular dynamics study. *Phys. Rev. E Stat. Nonlin. Soft Matter Phys.* 70: 051905.
50. Rapaport, D. C. 2008. Role of reversibility in viral capsid growth: a paradigm for self-assembly. *Phys. Rev. Lett.* 101:186101.
51. Hagan, M. F., O. M. Elrad, and R. L. Jack. 2011. Mechanisms of kinetic trapping in self-assembly and phase transformation. *J. Chem. Phys.* 135:104115.
52. Ayton, G. S., and G. A. Voth. 2010. Multiscale computer simulation of the immature HIV-1 virion. *Biophys. J.* 99:2757–2765.

53. Chen, B., and R. Tycko. 2011. Simulated self-assembly of the HIV-1 capsid: protein shape and native contacts are sufficient for two-dimensional lattice formation. *Biophys. J.* 100:3035–3044.

54. Perlmutter, J. D., C. Qiao, and M. F. Hagan. 2013. Viral genome structures are optimal for capsid assembly. *eLife.* 2:e00632.

55. Elrad, O. M., and M. F. Hagan. 2010. Encapsulation of a polymer by an icosahedral virus. *Phys. Biol.* 7:045003.

56. Mahalik, J. P., and M. Muthukumar. 2012. Langevin dynamics simulation of polymer-assisted virus-like assembly. *J. Chem. Phys.* 136: 135101.

57. Zhang, R., and P. Linse. 2013. Icosahedral capsid formation by capsomers and short polyions. *J. Chem. Phys.* 138:154901.

58. Cooke, I. R., and M. Deserno. 2005. Solvent-free model for self-assembling fluid bilayer membranes: stabilization of the fluid phase based on broad attractive tail potentials. *J. Chem. Phys.* 123:224710.

59. Wales, D. J. 2005. The energy landscape as a unifying theme in molecular science. *Philos. Trans. A Math. Phys. Eng. Sci.* 363:357–377.

60. Fejer, S. N., T. R. James, …, D. J. Wales. 2009. Energy landscapes for shells assembled from pentagonal and hexagonal pyramids. *Phys. Chem. Chem. Phys.* 11:2098–2104.

61. Hamard-Peron, E., and D. Muriaux. 2011. Retroviral matrix and lipids, the intimate interaction. *Retrovirology.* 8:15.

62. Johnson, M. C., H. M. Scobie, …, V. M. Vogt. 2002. Nucleic acid-independent retrovirus assembly can be driven by dimerization. *J. Virol.* 76:11177–11185.

63. Baumgärtel, V., S. Ivanchenko, …, D. C. Lamb. 2011. Live-cell visualization of dynamics of HIV budding site interactions with an ESCRT component. *Nat. Cell Biol.* 13:469–474.

64. Anderson, J. A., C. D. Lorenz, and A. Travesset. 2008. General purpose molecular dynamics simulations fully implemented on graphics processing units. *J. Comput. Phys.* 227:5342–5359.

65. Nguyen, T. D., C. L. Phillips, …, S. C. Glotzer. 2011. Rigid body constraints realized in massively-parallel molecular dynamics on graphics processing units. *Comput. Phys. Commun.* 182:2307–2313.

66. Andersen, H. C. 1980. Molecular dynamics simulations at constant pressure and/or temperature. *J. Chem. Phys.* 72:2384.

67. Deserno, M. 2009. Mesoscopic membrane physics: concepts, simulations, and selected applications. *Macromol. Rapid Commun.* 30: 752–771.

68. Humphrey, W., A. Dalke, and K. Schulten. 1996. VMD: visual molecular dynamics. *J. Mol. Graph.* 14:27–38.

69. Lingwood, D., and K. Simons. 2010. Lipid rafts as a membrane-organizing principle. *Science.* 327:46–50.

70. Kerviel, A., A. Thomas, …, D. Muriaux. 2013. Virus assembly and plasma membrane domains: which came first? *Virus Res.* 171:332–340.

71. Parton, D. L., A. Tek, …, M. S. P. Sansom. 2013. Formation of raft-like assemblies within clusters of influenza hemagglutinin observed by MD simulations. *PLOS Comput. Biol.* 9:e1003034.

72. Ivanchenko, S., W. J. Godinez, …, D. C. Lamb. 2009. Dynamics of HIV-1 assembly and release. *PLoS Pathog.* 5:e1000652.

73. Hagan, M. F. 2014. Modeling viral capsid assembly. *Adv. Chem. Phys.* 155:1–68.

74. Balasubramaniam, M., and E. O. Freed. 2011. New insights into HIV assembly and trafficking. *Physiology (Bethesda).* 26:236–251.

75. Kivenson, A., and M. F. Hagan. 2010. Mechanisms of capsid assembly around a polymer. *Biophys. J.* 99:619–628.

76. Perlmutter, J. D., M. R. Perkett, and M. F. Hagan. 2014. Pathways for virus assembly around nucleic acids. *J. Mol. Biol.* 426:3148–3165.

77. Phillips, R. B., J. Kondev, …, H. Garcia. 2013. Physical Biology of the Cell, 2nd Ed. Garland Science, New York.

78. Lipowsky, R. 1993. Domain-induced budding of fluid membranes. *Biophys. J.* 64:1133–1138.

79. Zandi, R., P. van der Schoot, …, H. Reiss. 2006. Classical nucleation theory of virus capsids. *Biophys. J.* 90:1939–1948.

80. Grant, J., R. L. Jack, and S. Whitelam. 2011. Analyzing mechanisms and microscopic reversibility of self-assembly. *J. Chem. Phys.* 135: 214505.

81. Rapaport, D. C. 2010. Modeling capsid self-assembly: design and analysis. *Phys. Biol.* 7:045001.

82. Becalska, A. N., C. F. Kelley, …, A. A. Rodal. 2013. Formation of membrane ridges and scallops by the F-BAR protein Nervous Wreck. *Mol. Biol. Cell.* 24:2406–2418.

83. Thiam, A. R., B. Antonny, …, F. Pincet. 2013. COPI buds 60-nm lipid droplets from reconstituted water-phospholipid-triacylglyceride interfaces, suggesting a tension clamp function. *Proc. Natl. Acad. Sci. USA.* 110:13244–13249.

84. Manneville, J.-B., J.-F. Casella, …, B. Goud. 2008. COPI coat assembly occurs on liquid-disordered domains and the associated membrane deformations are limited by membrane tension. *Proc. Natl. Acad. Sci. USA.* 105:16946–16951.

85. Jones, C. T., L. Ma, …, R. J. Kuhn. 2003. Flavivirus capsid is a dimeric $\alpha$-helical protein. *J. Virol.* 77:7143–7149.

86. Yue, T., and X. Zhang. 2011. Molecular understanding of receptor-mediated membrane responses to ligand-coated nanoparticles. *Soft Matter.* 7:9104.

87. Weikl, T. R., M. M. Kozlov, and W. Helfrich. 1998. Interaction of conical membrane inclusions: effect of lateral tension. *Phys. Rev. E.* 57:6988–6995.

88. Semrau, S., T. Idema, …, C. Storm. 2009. Membrane-mediated interactions measured using membrane domains. *Biophys. J.* 96:4906–4915.

89. Reynwar, B. J., and M. Deserno. 2011. Membrane-mediated interactions between circular particles in the strongly curved regime. *Soft Matter.* 7:8567–8575.

90. Goulian, M., R. Bruinsma, and P. Pincus. 1993. Long-range forces in heterogeneous fluid membranes. *Europhys. Lett.* 22:145–150.

91. McMahon, H. T., and J. L. Gallop. 2005. Membrane curvature and mechanisms of dynamic cell membrane remodeling. *Nature.* 438: 590–596.

92. Doherty, G. J., and H. T. McMahon. 2009. Mechanisms of endocytosis. *Annu. Rev. Biochem.* 78:857–902.

93. Taylor, M. P., O. O. Koyuncu, and L. W. Enquist. 2011. Subversion of the actin cytoskeleton during viral infection. *Nat. Rev. Microbiol.* 9:427–439.

94. Gladnikoff, M., E. Shimoni, …, I. Rousso. 2009. Retroviral assembly and budding occur through an actin-driven mechanism. *Biophys. J.* 97:2419–2428.

95. Cooke, I. R., K. Kremer, and M. Deserno. 2005. Tunable generic model for fluid bilayer membranes. *Phys. Rev. E Stat. Nonlin. Soft Matter Phys.* 72:011506.

96. Weeks, J. D., D. Chandler, and H. C. Andersen. 1971. Role of repulsive forces in determining the equilibrium structure of simple liquids. *J. Chem. Phys.* 54:5237.

97. Grest, G. S., and K. Kremer. 1986. Molecular dynamics simulation for polymers in the presence of a heat bath. *Phys. Rev. A.* 33:3628–3631.

98. Reynwar, B. J., and M. Deserno. 2008. Membrane composition-mediated protein-protein interactions. *Biointerphases.* 3:FA117.

99. Bereau, T., Z.-J. Wang, and M. Deserno. 2014. More than the sum of its parts: coarse-grained peptide-lipid interactions from a simple cross-parametrization. *J. Chem. Phys.* 140:115101.

# Simulations show that virus assembly and budding is facilitated by membrane microdomains

Teresa Ruiz-Herrero
*Departamento de Física Teórica de la Materia Condensada, Universidad Autónoma de Madrid, Madrid , Spain;*

Michael F. Hagan
*Martin Fisher School of Physics Physics, Brandeis University, Waltham, MA, 02454*
(Dated: January 13, 2015)

## S1. ADDITIONAL RESULTS FIGURES

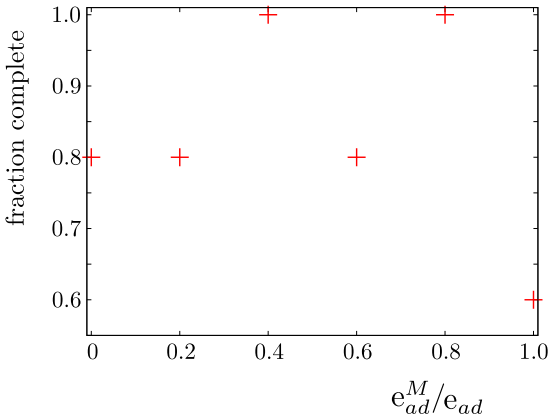


Figure S1. Results from simulations where the partitioning of subunits between the bulk membrane and domain is varied. The fraction of trajectories that led to complete assembly and budding is shown as a function of the ratio between subunit-lipid interaction strengths for bulk-membrane and domain lipids, $e^M_{\rm ad}/e_{\rm ad}$. Specifically, the subunit-membrane attraction strength for domain lipids is $e_{\rm ad} = 0.5\alpha$, while the subunit-membrane attraction strength for bulk membrane lipids is varied from $0 \leq e^M_{\rm ad} \leq 0.5\alpha$. The fraction of trajectories leading to complete assembly was estimated from five independent simulations for each value of $e^M_{\rm ad}$. The mean completion time $\bar{\tau}$ was also not sensitive to the degree of partitioning for $e^M_{\rm ad}/e_{\rm ad} < 1$ ($\bar{\tau} = 6\cdot 10^6 \tau_0$); however, the mean completion time for $e^M_{\rm ad} = e_{\rm ad} = 1$ was an order of magnitude longer ($\bar{\tau} = 4\cdot 10^7 \tau_0$). Other parameter values were fixed at: $e^D_{\rm ad} = 0.5\alpha$, $r_{\rm domain} = 35\sigma$ and $\epsilon_D/\epsilon_0 = 0.85$ ($\gamma \approx 1.9 k_{\rm B}T/\sigma$). Trajectories were run until budding or until a mis-assembled structure such as those shown in Fig. S13 was identified.

## S2. METHODS

Our model is defined by pairwise potentials, and the total interaction energy $U_{\rm TOT}$ can be separated into three parts:

$$U_{\rm TOT} = \sum_{\text{M-M pairs}} U_{\rm MM} + \sum_{\text{C-C pairs}} U_{\rm CC} + \sum_{\text{M-C pairs}} U_{\rm MC}, \tag{S1}$$

with $U_{\rm MM}$, $U_{\rm CC}$, and $U_{\rm MC}$ defining interactions between pairs of membrane beads, capsomer beads, and membrane-capsomer pairs respectively. These potentials are defined in sections S2 A-S2 C, and the parameter values are listed in section S2 D.

### A. The membrane model

We model the amphiphilic lipids comprising the membrane with a coarse grained implicit solvent model from Cooke et al [1], in which each amphiphile is represented by one head bead and two tail beads. The interaction

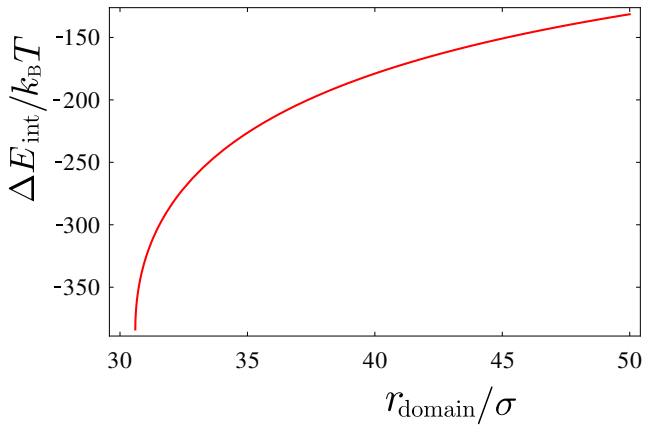


Figure S2. Change in interfacial energy between a flat domain and a completely wrapped capsid (Eq. 2 main text) as a function of the domain radius.

between membrane particles consists of four parts:

$$U_{\rm MM}(r) = U_{\rm WCA} + U_{\rm bond} + U_{\rm bend} + U_{\rm hydro}. \tag{S2}$$

Every pair of membrane beads interacts via a repulsive Weeks-Chandler-Andersen potential [2]:

$$\begin{aligned} U_{\rm WCA}(r, b_{ij}) =& 4\epsilon_0 \left[ \left(\frac{b_{ij}}{r}\right)^{12} - \left(\frac{b_{ij}}{r}\right)^{6} + \frac{1}{4} \right] && ; r \le r_{\rm c} \\ & 0 && ; r > r_{\rm c} \\ & i, j \in \{\text{head,tail}\} \end{aligned} \tag{S3}$$

with $r_{\rm c} = 2^{1/6} b_{ij}$ and $b_{ij}$ chosen to ensure an effective cylindrical lipid shape: $b_{\text{head-head}} = b_{\text{head-tail}} = 0.95\sigma_0$ and $b_{\text{tail-tail}} = \sigma_0$, where $\sigma_0$ will turn out to be the typical distance between beads within a model lipid molecule.

The beads belonging to a given lipid are connected through FENE bonds (Eq. (S4)) [3] with maximum length $r_{\rm cut} = 1.5\sigma$, and the linearity of the molecule is achieved via a harmonic spring with rest length $4\sigma$ between the first and the third bead, Eq. (S5)

$$U_{\rm bond}(r) = -\frac{1}{2}\kappa_{\rm bond} r_{\rm cut}^2 \ln\left[1 - (r/r_{\rm cut})^2\right] \tag{S4}$$

$$U_{\rm bend}(r) = \frac{1}{2}\kappa_{\rm bend}\left(r - 4\sigma_0\right)^2 \tag{S5}$$

Since this is an implicit solvent model, hydrophobicity is represented by an attractive interaction, Eq. (S6), between all tail beads. The molecules belonging to the domain are labeled $D$, while those forming the rest of the membrane are referred to as $M$. The interaction between molecules of the same type is the same for $D$ or $M$, but the strength of the effective hydrophobic interaction between molecules of different type is lower:

$$U^{ij}_{\rm hydro}(r) = \begin{cases} -\epsilon_{ij} & ; \quad r < r_{\rm c} \\ -\epsilon_{ij}\cos^2\frac{\pi(r-r_{\rm c})}{2\omega_{\rm c}} & ; \; r_{\rm c} \le r \le r_{\rm c} + \omega_{\rm c} \\ 0 & ; \quad r > r_{\rm c} + \omega_{\rm c} \end{cases} \tag{S6}$$

where the interaction between the molecules of the same type is given by $\epsilon_{\rm DD} = \epsilon_{\rm MM} = \epsilon_0$, and the cross term, $\epsilon_{\rm DM}$, is a parameter that controls the strength of the line tension between domains. Varying $\epsilon_{\rm DM}$ from 0 to $\epsilon_0$ tunes the line tension, from a large value to 0. The energy of the domain border is proportional to the line tension and the domain perimeter, Eq. (S7)

$$E_{\rm int} = 2\pi r_{\rm domain}\gamma \tag{S7}$$

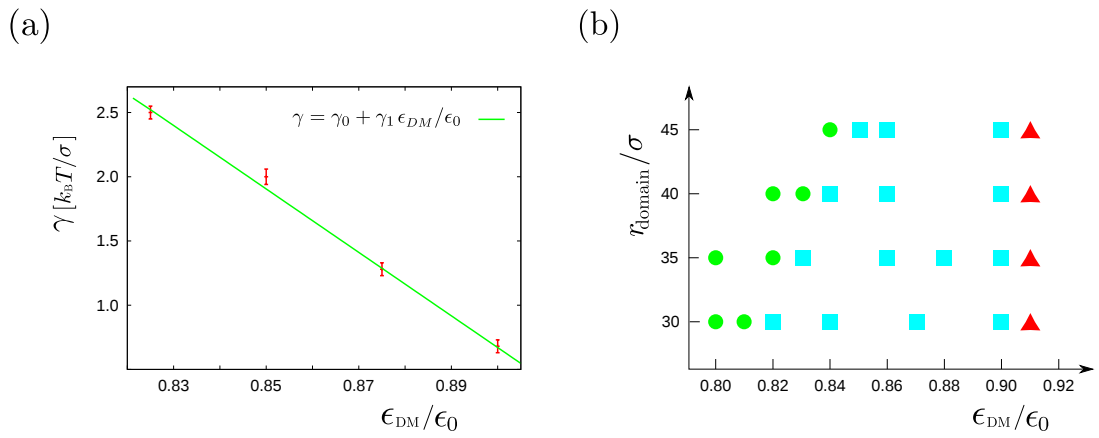


Figure S3. **(a)** Approximate line tension calculated from the observed phase boundary for budding of the domain. The solid line is a linear fit to the data (Eq. (S9)). **(b)** Phase diagram of the domain behavior as a function of the domain radius and line tension ($\gamma\sigma/k_BT \approx 22.9 - 24.7\epsilon_{DM}/\epsilon_0$) obtained from molecular dynamics simulations of a membrane with a domain at $k_BT = 1.1\epsilon_0$. The possible outcomes are indicated as: domain dissolution (▲), domain in equilibrium with the membrane (■), and spontaneous budding of the whole domain (●).

where $r_{\text{domain}}$ is the domain radius and $\gamma$ the line tension. We calculated the interfacial energy following Ref. [5]. We set up a bilayer in the xy plane with an interface parallel to the y-axis (there are thus two interfaces due to the periodic boundaries); *i.e.*, in the initial configuration membrane contained solely M molecules for $y < 0$ and solely D molecules for $y > 0$. In this geometry the line tension can be calculated as the difference between the normal and tangent components of the pressure tensor to the interface, multiplied by the area where this pressure acts ($L_xL_z$) and divided by the number of interfaces [5]:

$$\gamma = (p_{yy} - p_{xx})\frac{L_xL_z}{2} \tag{S8}$$

We calculated the line tension for different values of $\epsilon_{DM}$, and obtained a linear relation between the line tension and the attractive interaction strength between lipid molecules of different types (Fig. S3a)

$$\gamma = \gamma_0 + \gamma_1(\epsilon_{DM}/\epsilon_0) \tag{S9}$$

with $\gamma_0 = 22.9k_BT/\sigma$ and $\gamma_1 = -24.7k_BT/\sigma$.

To characterize the dynamics of the domain as a function of the line tension, we also ran simulations of bilayers initialized with circular domains and different values of $r_{\text{domain}}$ and $\gamma$. For a given value of $r_{\text{domain}}$, as $\gamma$ is increased the equilibrium state transitions from a homogeneous membrane to a phase-separated but stable membrane to budding of the entire domain (Fig. S3b). These results are qualitatively consistent with the theoretical relationship between line tension and the domain size which is unstable to budding derived in Ref. [4]. However, the simulated line tensions required for budding are larger than the theoretical value for spontaneous budding, suggesting that simplifications in the theory lead to underestimation of the free energy barrier to budding.

### B. The capsid subunit model

Our model for capsid assembly is based on the model for $T$=1 capsids developed by Wales [6], but has been extended to allow interactions with the membrane. Our capsid subunit is a rigid body with a pentagonal base and radius of $r_{\text{pentamer}} = 5\sigma$ formed by 15 attractive and 10 repulsive interaction sites. The interaction between capsomers consists of an attractive potential that promotes assembly and a repulsive interaction between specific beads that drives formation of the capsid geometry, Eq.(S10)

$$U_{\text{CC}} = U_{\text{att}} + U_{\text{rep}} \tag{S10}$$

While the original model [6] contained 5 attractive and 5 repulsive sites, the new sites that we have added (Figs. S4a and S4b) are necessary to describe assembly on a fluctuating surface. The effects of their inclusion are shown in the following sections.

### 1. Attractor sites

Subunit assembly is mediated through a Morse potential between 'attractor' pseudoatoms located in the pentagon plane, with one located at each subunit vertex and 2 along each edge. Attractions occur between like attractors only, meaning that there are vertex-vertex and edge-edge attractions, but no vertex-edge attractor interactions, Eq. (S11)

$$\begin{aligned} U_{\mathrm{att}} = \epsilon^{\mathrm{v}}_{\mathrm{att}} \sum_m \sum_n \left( e^{\rho(1-R_{mn}/R_{\mathrm{e}})} - 2 \right) e^{\rho(1-R_{jk}/R_{\mathrm{e}})} \\ + \epsilon^{\mathrm{e}}_{\mathrm{att}} \sum_p \sum_q \left( e^{\rho(1-R_{pq}/R_{\mathrm{e}})} - 2 \right) e^{\rho(1-R_{lm}/R_{\mathrm{e}})} \end{aligned} \tag{S11}$$

where $R_{mn}$ is the distance between sites $m$ and $n$,with $m$ running over the attractor sites on the vertices of the first capsomer , and $n$ running over the vertices on the second. $R_{pq}$ is the analogous distance between the edge sites on each of the capsomers. $R_{\mathrm{e}}$ is the equilibrium pair distance and $\rho$ defines the range of the interaction. Finally, $\epsilon^{\mathrm{v}}_{\mathrm{att}}$ and $\epsilon^{\mathrm{e}}_{\mathrm{att}}$ are the interaction strengths between vertex and edge sites respectively; we set $\epsilon^{\mathrm{e}}_{\mathrm{att}} = 0.5\epsilon^{\mathrm{v}}_{\mathrm{att}}$ because there are two edge beads per vertex bead.

In comparison to the original model [6] the additional attractive sites provide a stronger driving force for formation of structures with the lowest energy face-face angles and thus provide additional thermodynamic stabilization of the lowest energy dodecahedron capsid structure. This increased stabilization of the curved, icosahedral shape is necessary to compete with membrane bending energy which favors flat aggregates. Although we did observe assembly on the membrane with the original model for carefully tuned parameters, the improved model undergoes assembly over a wider range of parameter values.

### 2. Repulsive sites

The 10 repulsive interaction sites are separated into 5 'top' and 5 'bottom' sites, which are arranged symmetrically above and below the pentagon plane respectively, so as to favor a subunit-subunit angle consistent with a dodecahedron (116 degrees). They are at distance $h$ from the capsomer plane, and their projections on that plane lie on each of the pentamer radii, at a distance $l$ to the corner. The ratio $h/l$ is the same as in the original model (Fig. S4b and Fig. S4c). The interaction potential between top and bottom sites on two capsomers is similar to that in the original model but extended to all the sites:

$$U_{\mathrm{rep}} = \epsilon_{\mathrm{rep}} \sum_{i=1}^{5} \sum_{j=1}^{5} \left( \frac{\sigma_{\mathrm{t}}}{R_{ij}} \right)^{12} + \epsilon_{\mathrm{rep}} \sum_{m=1}^{5} \sum_{n=1}^{10} \left( \frac{\sigma_{\mathrm{b}}}{R_{mn}} \right)^{12} \tag{S12}$$

where $R_{ij}$ is the distance between the top sites, with $i$ and $j$ running over the 5 top sites of each of the capsomers, and $R_{mn}$ is the distance between $m$ and $n$, with $m$ running over the bottom sites of the first capsomer and $n$ running over the top and bottom sites of the second one. $\sigma_{\mathrm{t}}$ is, as in the original model, the distance between two adjacent top sites in a complete capsid at its lowest energy configuration, and is obtained from the geometry depicted in Fig. S4c:

$$\sigma_{\mathrm{t}} = 2d\sqrt{\frac{1}{10}\left(5+\sqrt{5}\right)} + 2h\sqrt{\frac{1}{10}\left(5-\sqrt{5}\right)} + R_{\mathrm{e}} \tag{S13}$$

where $d = l\sin(3\pi/10)$. Similarly, $\sigma_{\mathrm{b}}$ was initially set to the distance between the top and bottom sites of two adjacent capsomers in a complete capsid, but then was adjusted to $\sigma_{\mathrm{b}} = 0.75\sigma_{\mathrm{t}}$ to optimize assembly behavior.

We changed the form of the repulsive sites in the original model (one top and one bottom site) to 5 sites for the following reasons. From exploratory simulations, we found that membrane-subunit interactions significantly constrained relative orientations of nearby adsorbed subunits for physically relevant values of the membrane bending modulus. Therefore, association can proceed only through a relatively narrow range of face-face angles (in comparison to the angles available for association in solution). As the partial capsid grows, the accessible range of angles narrows even further (Fig. S6a). Increasing the number of repulsive sites and moving them closer to the capsomer plane enables a decrease in the interaction range, which allows a wider range of approach angles while maintaining the equilibrium angle at the same value as for the original model. Moreover, the reduction of the interaction cutoff reduced computation times by nearly a factor of 3.

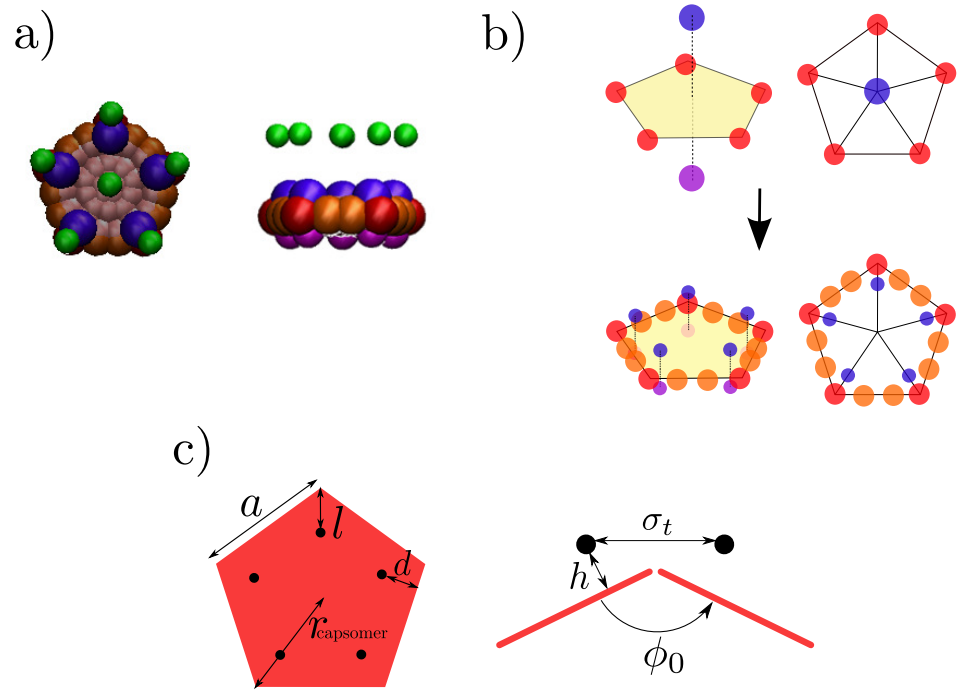


Figure S4. **(a)** Top and side view of the model capsomer, with attractor sites in red and orange, top and bottom repulsive sites in violet and magenta, excluders in pink, and membrane-capsomer interaction sites in green. **(b)** Comparison of the original model [6] and our extended model. Orange circles represent the new attractive sites on the capsomer edges, and the blue and purple circles denote the new repulsive sites. **(c)** Capsomer geometry in the extended subunit model. (Left): a top view of a capsomer of radius $r_{\text{pentamer}}$ and edge length $a$. The projections of the new repulsive sites on the capsomer plane lie on each of the pentamer radii, at distances $l$ from the nearest vertex and $d$ from the pentamer edge. Their distances from the capsomer plane, $h$, and $l$ keep the same proportions as those in the original model. (Right): Geometry of capsomer-capsomer binding. For two adjacent pentamers in a complete capsid, the distance between two opposite repulsive sites is $\sigma_{\text{t}}$ and the equilibrium angle is $\phi_0$

### C. Subunit-membrane interactions

The potential between capsomers and lipids is split into parts accounting for attractive and excluded-volume interactions respectively: $U_{\text{MC}} = U_{\text{ad}} + U_{\text{ex}}$. These are defined as follows.

#### *1. Adhesion interaction sites*

The attractive subunit-membrane interaction is mediated by six sites, one at each of the five vertices and one at the center of the capsomer. Each site sits at a distance $L_{\text{s}}$ from the pentamer plane (Fig. S4a). These new interaction sites interact only with the tails of the lipid molecules. In simulations with a domain, the sites interact only with domain lipid tails (except for Fig. S1). The attractor-tail interaction is the same as the tail-tail interaction except that there is no repulsive component, as if the attractors were point-particles with no excluded volume:

$$U_{\text{ad}}(r) = \begin{cases} -\epsilon_{\text{ad}} & ; \quad r < r_{\text{c}} \\ -\epsilon_{\text{ad}} \cos^2 \frac{\pi(r-r_{\text{c}})}{2\omega_{\text{c}}} & ; \quad r_{\text{c}} \le r \le r_{\text{c}} + \omega_{\text{c}} \\ 0 & ; \quad r > r_{\text{c}} + \omega_{\text{c}} \end{cases} \tag{S14}$$

where $r$ is the distance between a capsomer adhesion site and the tail bead of a lipid. This form of interaction led to a relatively smooth energy surface for diffusion of adsorbed subunits (in contrast to versions of the model in which we constructed attractive interactions with lipid head groups).

### 2. Excluder sites

A layer of 35 beads arranged in the shape of a pentagon is added to the capsomer base to prevent the overlap of capsid subunits and membrane lipids (Fig. S4a). These beads interact via an excluded volume potential $U_{\rm ex}$ with all lipid beads:

$$U_{\rm ex}(r) = \begin{cases} 4\epsilon_0 \left[ \left(\frac{\sigma}{r-s}\right)^{12} - \left(\frac{\sigma}{r-s}\right)^{6} + \frac{1}{4} \right] & ; r \leq s + r_{\rm c} \\ 0 & ; r > s + r_{\rm c} \end{cases} \tag{S15}$$

with $s = (\sigma_{\rm ex} + \sigma)/2 - 1$, and $\sigma_{\rm ex}$ as the size of the excluders. In this way, the effective shape of the capsomer is a regular pentagon with thickness $\sigma_{\rm ex}$.

### 3. Adhesion energy

The adhesion free energy per capsomer was estimated from the calculation of the interaction between a matrix protein attractive site and the lipid tail beads lying inside its interaction range. The number of interacting beads depends on the matrix protein penetration into the membrane (Fig.S5a), so the free energy was integrated over the accessible values of the penetration $p$:

$$F = -k_{\rm B}T \ln \left( \frac{\int_{p_{\rm min}}^{p_{\rm max}} e^{-E(p)} dp}{v_0^{1/3}} \right). \tag{S16}$$

where $v_0 = (\Delta p \pi r_{\rm cut}^2)$ is the standard volume, $\Delta p$ the range of possible penetrations where capsomer adhesion sites experience attractive interactions with the membrane, and $E(p)$ the interaction energy for a given penetration:

$$E(p) = 6\rho \int_{z_{\rm min}(p)}^{z_{\rm max}(p)} {\rm d}z \int_0^{R_{\rm max}(z)} U(\vec{r} - p) 2\pi r dr \tag{S17}$$

with $\rho$ the density of lipid tails and 6 standing for the number of interaction sites per capsomer. The geometry of the system used for the integration is shown in Fig.S5b

We found that the adhesion free energy per unit area is linearly related to $\epsilon_{\rm ad}$:

$$e_{\rm ad} \approx \alpha \epsilon_{\rm ad} \tag{S18}$$

with $\alpha = -2.276\sigma^{-2}$. Note that this estimate overestimates the adsorption free energy, since it does not include entropy losses suffered by lipid molecules upon subunit adsorption. Finally, we note that in principle the magnitude and form of subunit-lipid interactions could be parameterized from higher resolution models (e.g. [7]).

## D. Parameters

The units of energy, length, and time in our simulations were respectively $\epsilon_0$, $\sigma$ and $\tau_0$. The parameters for the membrane are chosen from Ref. [8] so that the bilayer is in a fluid state. We set the temperature of our simulations to $k_{\rm B}T/\epsilon_0 = 1.1$ and the lipid-lipid interaction range to $\omega_{\rm c} = 1.5\sigma$, both in equation (S6) and equation (S14). The bending rigidity for these values is $\kappa = 8.25 k_{\rm B}T$ and the areal density of lipids $\eta = 0.768\sigma^{-2}$ .

The parameters for the virus model were set according to the phase diagrams of the original model [9, 10] and our exploratory simulations of assembly on a membrane. We found that the optimal parameters that allow large assembly yields for a wide range of concentrations for $k_{\rm B}T/\epsilon_0 = 1.1$ are: $R_{\rm e} = 1\sigma$, $r_{\rm pentamer} = 5\sigma$, $\rho = 3$, $h = 0.9375\sigma$, $l = 1.25\sigma$, $\sigma_{\rm t} = 2.63\sigma$, $\sigma_{\rm b} = 0.75\sigma_{\rm t}$, $L_{\rm s} = 6\sigma$, $\epsilon_{\rm att}^{\rm v} = 11.6\epsilon_0 = 10.55 k_{\rm B}T$, $\epsilon_{\rm att}^{\rm e} = 5.8\epsilon_0 = 5.27 k_{\rm B}T$, and $\epsilon_{\rm rep} = 0.261\epsilon_0$. The values of the capsid parameters were chosen so that the total energy of assembly exceeds the bending energy of wrapping the capsid. The energy needed for assembly on the membrane is above the optimal energy for bulk assembly, a higher energy is needed to induce membrane curvature without capsid disassembly. Finally, the thickness of the capsomer is $\sigma_{\rm ex} = 1.25\sigma_0$, and the total mass of a capsomer is $m_{\rm pentamer} = 66 m_0$.

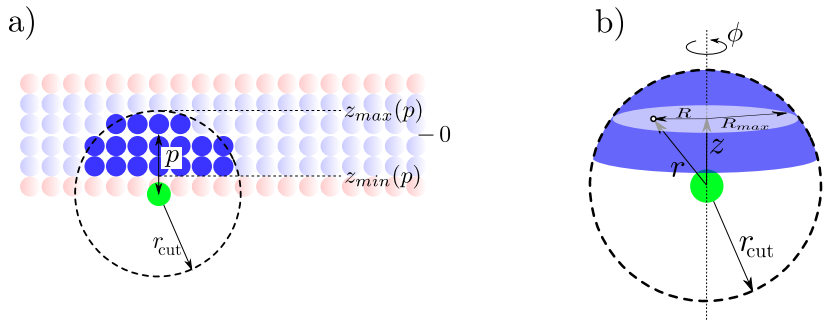


Figure S5. Geometry used for the calculation of the adhesion energy. **a)** The schematic shows a slice of a membrane with the interaction point representing the matrix protein in green at a given penetration $p$. The lipid tails are represented in blue and the heads in red. The tail beads that lie inside the matrix protein interaction volume $V_{\text{int}}$ are showed in solid blue and they are confined between $z_{\text{max}}$ and $z_{\text{min}}$ in the z-direction. The potential cutoff is given by $r_{\text{cut}} = r_c + \omega_c$. **b)** Geometry used for the integration of the adhesion energy . The energy contribution of every point inside a disk of radius $R_{\text{max}}(z)$ and width dz is integrated inside the interaction volume (represented in blue).

The velocity and position of each lipid pseudo-atom $i$, with mass $m_0$, evolves according to Nosé-Hoover barostat with coupling constants for the thermostat $\tau = 0.4\tau_0$ and for the barostat $\tau_p = 0.5\tau_0$. The dynamics of lipid pseudo-atoms were simulated using the npt algorithm in HOOMD (version 0.10.1) [11, 12].

Capsomers in turn, are represented by rigid bodies of mass $m_{\text{pentamer}}$. The center of mass of capsomer $i$ follows Langevin equation (Eq. S19) according to the total force acting on it, $f_i = -\Delta V^i_{\text{TOT}}$, the thermal noise at temperature $T$, and the friction coefficient $\xi_{\text{trans}}$.

$$m_{\text{pentamer}}\ddot{\boldsymbol{r}}_{\boldsymbol{i}} = \boldsymbol{f}_i - \xi_{\text{trans}}\dot{\mathbf{r}} + \sqrt{2\xi_{\text{trans}}k_{\text{B}}T}\boldsymbol{R}(t) \tag{S19}$$

Capsomer orientations evolved according to the Langevin equation for rotational motion Eq.S20

$$\boldsymbol{I}\cdot\dot{\boldsymbol{\Omega}} = \boldsymbol{\tau}_i - \xi_{\text{rot}}\boldsymbol{\Omega} + \sqrt{2\xi_{\text{rot}}k_{\text{B}}T}\boldsymbol{R}(t) \tag{S20}$$

where $\boldsymbol{\Omega}_i$ is the angular velocity of capsomer $i$, $\boldsymbol{\tau}_i$ is the total torque acting on it, $\boldsymbol{I}$ is the moment of inertia of a capsomer, and $\xi_{\text{rot}}$ is the rotational friction coefficient. The equations of motion were simulated using the bdnvt_rigid algorithm in HOOMD [11, 12], modified so that forces and torques arising from drag and random buffeting were applied separately and isotropically. In the simulations the following magnitudes were used: $I_z = 870m_0\sigma^2$, $I_x \sim I_y = 205m_0\sigma^2$, $\xi_{\text{trans}} = 1.31m_0/\tau$, $\xi_{\text{rot}} = 2.6k_{\text{B}}T\tau_0$. Note that for these parameters the rotational motion for particles in bulk is not as overdamped as would be the case for a protein in water. We performed additional simulations in which the friction constant was increased to $100k_{\text{B}}T\tau_0$ and $1\cdot10^4k_{\text{B}}T\tau_0$. Behavior in the simulations with $\xi_{\text{rot}} = 100k_{\text{B}}T\tau_0$ was unchanged, while for $\xi_{\text{rot}} = 1\cdot10^4k_{\text{B}}T\tau_0$ instances of bonding between inverted particles were observed. This mis-bonding is a known artifact of this model, which can be eliminated by including additional pseudo-atoms [10].

The remaining parameters can be assigned physical values by setting the system to room temperature, $T = 300K$, and noting that the typical width of a lipid bilayer is around 5 nm, and the mass of a typical phospholipid is about 660 g/mol. The units of our system can then be assigned as follows: $\sigma = 0.9$ nm, $m_0 = 220$ g/mol, $\epsilon_0 = 3.77\times10^{-21}$J $= 227\text{g}\text{Å}^2/\text{ps}^2\text{mol}$, and $\tau_0 = \sigma\sqrt{m_0/\epsilon} = 8.86$ ps.

## S3. THEORETICAL ANALYSIS ON THE EFFECT OF THE DOMAIN ON NECK GEOMETRY

The main barrier for assembly on homogeneous membranes arises because strong curvature in the rim (neck) region inhibits capsomers from diffusing to the budding sites. Here we estimate parameter values for which the presence of a domain will lead to long necks with small curvatures that facilitates subunit diffusion. Specifically, there is a threshold curvature $c^*$, determined by the geometry of the capsomer (Fig. S7), beyond which the subunit-membrane attraction must decrease. For our system $c^* = 3/17\sigma^{-1}$, which corresponds to a minimum radius of curvature $r^* = 17/3\sigma$.

In the case of a homogeneous membrane, the curvature in the rim region depends on the bending modulus $\kappa$ and adhesion energy $e_{\text{ad}}$: strong adhesion energy and small bending modulus leads to a tightly wrapped capsid and thus

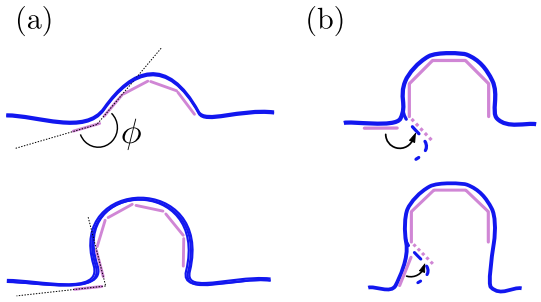


Figure S6. Geometry of the membrane during simultaneous assembly and budding. **(a)** As budding proceeds, the angle between the growing capsid and the associating capsomers becomes more acute. In the original model the long-range repulsions between top beads do not allow sufficient orientational flexibility for capsomers to approach at such acute angles. **(b)** Association of a subunit adsorbed on the membrane requires either attachment of the subunit or a local membrane conformational change. **(top)** A short neck formed around a large partial-capsid intermediate leads to a strong kink and thus association of another subunit requires a significant membrane deformation. **(bottom)** A long neck, such as found during assembly of a raft with optimal size, leads to a soft kink and subunit association involves relatively modest membrane deformations.

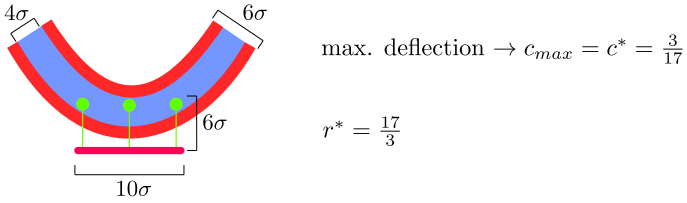


Figure S7. Maximum membrane curvature $c^*$ that allows capsomers diffusion with no energy barrier; for simplicity we assume that subunit-membrane attractors (green) are aligned with a principle axis.

high curvature in the rim. From these parameters we can define a relaxation length $l_r \sim \sqrt{\kappa/\epsilon_{ad}}$, with $\epsilon_{ad}$ the adhesion energy per unit area. For our calculation, we approximate the neck (rim) region as a section of a toroid, with a curvature related to the relaxation length as $c = \frac{\pi}{2l_r}$ (Fig. S7) [13]. The annular area of the domain between the edge of the rim and the domain interface is approximated as flat.

Now, we consider the case of a half-capsid, which is the size at which assembly typically stalls on a homogeneous

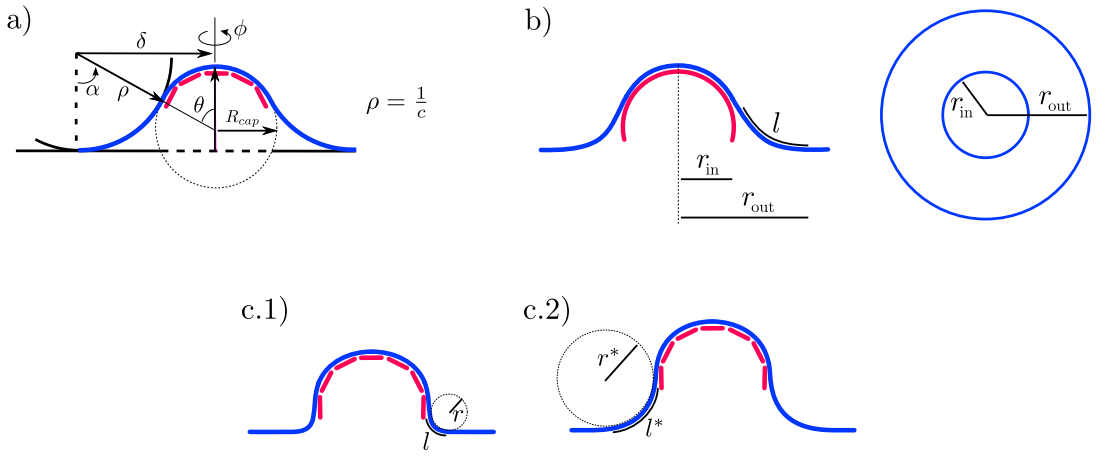


Figure S8. **(a)** Toroid approximation for the rim. $\rho$ is a function of $l$ via the curvature $c(l)$. **(b)** Definition of domain radius after membrane deformation during wrapping. **(c)** Membrane shape. c.1) approximated shape adopted by the membrane with no domain and relaxation length $l$, c.2) Membrane shape with the maximum curvature ($c^*$) that allows particle diffusion.

membrane, and we compare the energy of a short neck typical of a homogeneous membrane with $c = \frac{\pi}{2l_r}$ (Fig. S8c.1) with the long shallow neck that facilitates subunit diffusion, with $c = c^*$ (Fig. S8c.2). We observe from simulations that longer necks require partial detachment of the membrane by approximately 25% of the membrane attractors on subunits at the perimeter of the capsid intermediate. The change in adhesion energy between these two configurations is then given by

$$\Delta E_{\text{ad}} = E_{\text{ad}}(\text{long neck}) - E_{\text{ad}}(\text{short neck}) = f e_{\text{ad}} \Delta A_{\text{attached}} \sim e_{\text{ad}} 2\pi R_{\text{capsid}} f r_{\text{pentamer}} \tag{S21}$$

with $f = 0.25$, $2\pi R_{\text{capsid}} f r_{\text{pentamer}}$ accounts for 25% of the capsomer area of the outer ring of the half capsid being detached from membrane attractors.

Next, since we are assuming that the rim region corresponds to a section of a toroid, its bending energy is calculated as [13]

$$E_{\text{bend}}^{\text{rim}} = \pi\kappa \int_0^{\pi/2} \rho(\delta - \rho\sin\alpha) \left(\frac{1}{\rho} - \frac{\sin\alpha}{\delta - \rho\sin\alpha}\right)^2 d\alpha \tag{S22}$$

where $\rho$ and $\delta$ are functions of the rim curvature $c(l)$ as shown in Fig. S8a, and since we consider a half-capsid, the membrane detaches at angle $\theta = \pi/2$. The change in bending energy between long and short necks is then given by

$$\Delta E_{\text{bend}} = E_{\text{bend}}^{\text{rim}} \left(l^* = \frac{\pi}{2c^*}\right) - E_{\text{bend}}^{\text{rim}} \left(l_{\text{r}} = \sqrt{\frac{\kappa}{\epsilon_{\text{ad}}}}\right). \tag{S23}$$

Finally, the formation of a long neck is driven by a corresponding reduction in the interfacial energy. We calculate the interfacial energy following Eq. 2 (main text) extended to include the effect of the rim geometry. Assuming that the total area of the domain $A_{\text{domain}} = \pi r_{\text{domain}}^2$ is conserved, the area of the flat annular region between the edge of the rim and the domain interface (Fig.S8b) is given by

$$A_{\text{flat}} = \pi(r_{\text{out}}^2 - r_{\text{in}}^2) = A_{\text{domain}} - A_{\text{wrap}} - A_{\text{rim}}(l) \tag{S24}$$

where $r_{\text{out}}$ is the radius of the domain in the plane of the membrane, $r_{\text{in}} = R_{\text{capsid}} \sin\theta$ is the in-plane radius of the wrapped capsid intermediate, $A_{\text{wrap}} = 2\pi R_{\text{capsid}}^2(1 - \cos\theta)$ is the area of the wrapped intermediate, and $A_{\text{rim}}(l)$ is the rim area which depends on the relaxation length $l_{\text{r}}$ or $l^*$. The change in interfacial energy between states a) and b) is then:

$$\Delta E_{\text{int}} = 2\pi\gamma \left[r_{\text{out}}(l^*) - r_{\text{out}}(l_{\text{r}})\right] \tag{S25}$$

with

$$r_{\text{out}}(l) = r_{\text{domain}} \sqrt{1 - \frac{R_{\text{capsid}}^2 + \left(2 + \frac{4}{\pi}\right) l R_{\text{capsid}} + \left(\frac{4}{\pi} - \frac{12}{\pi^2}\right) l^2}{r_{\text{domain}}^2}}. \tag{S26}$$

From Eq. S26 we immediately see that that when $r_{\text{domain}}^2 \gg R_{\text{capsid}}^2$, $r_{\text{out}}$ is nearly constant. Thus the interface of a large domain provides insufficient driving force to promote a long neck; similar to the finding that the interfacial driving force for membrane curvature decreases the domain size (Eq. 2).

Finally, the total change in energy between a short neck and a long neck is given by $\Delta E = \Delta E_{\text{ad}} + \Delta E_{\text{bend}} + \Delta E_{\text{int}}$ (Eqs. S21, S23 and S25). Negative values of $\Delta E$ indicate that the long neck is favorable and thus assembly is likely to proceed past the half-capsid state in the presence of the domain. The dependence of $\Delta E$ on $r_{\text{domain}}$, $e_{\text{ad}}$, and $\gamma$ is shown in Fig. S9. We see that the results qualitatively match the behavior observed in the simulations; moderate values of $e_{\text{ad}}$ and domain sizes larger than but comparable to the capsid area are required to promote assembly and budding.

## S4. ADDITIONAL FIGURES

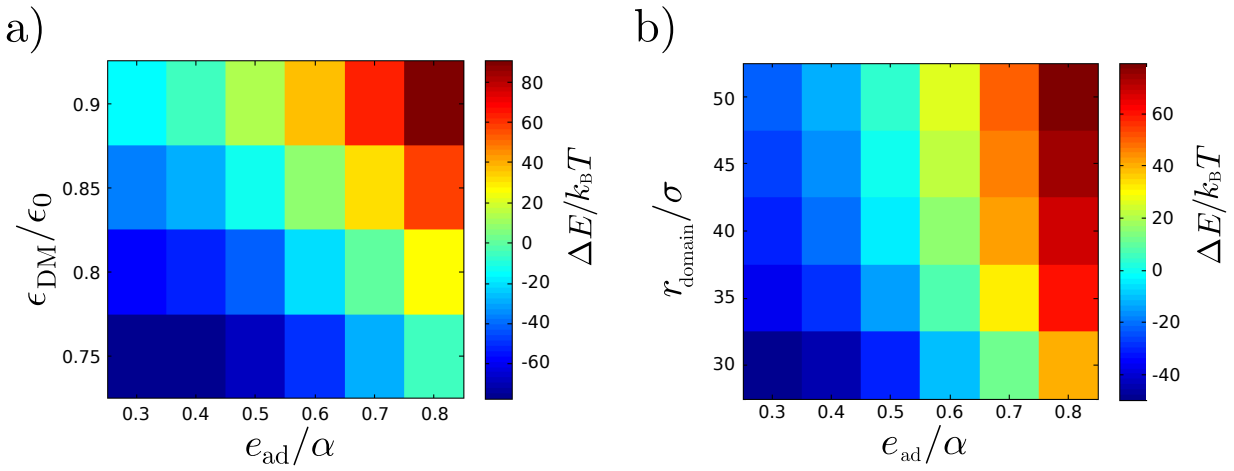


Figure S9. Difference in total energy between a long and short neck ($\Delta E = E(\text{long-neck}) - E(\text{short neck})$ as a function of **(a)** line tension ($\gamma\sigma/k_BT \approx 22.9 - 24.7\epsilon_{DM}/\epsilon_0$) and adhesion strength, and **(b)** domain radius and adhesion strength. Positive energies in red show that the system will not adopt the softer configurations needed for assembly to proceed beyond a half-capsid.

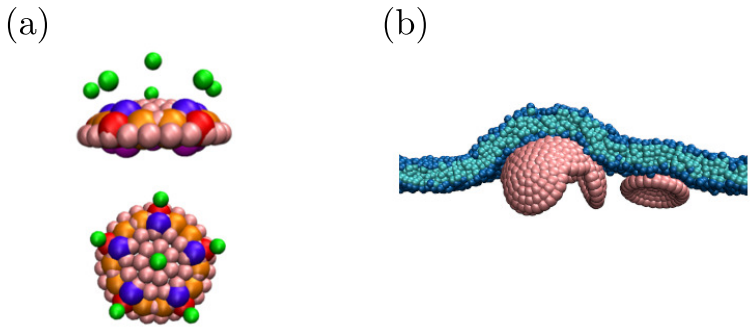


Figure S10. Curved capsomer model. (a) Top and side view of the capsomer. Sites are the same as for the planar subunit; attractive sites are red and orange, top and bottom repulsive sites are blue and purple, excluders are pink, and capsomer-lipid interaction sites are green. (b) On a homogenous membrane, assembly stalls at the half capsid, as found for the planar case.

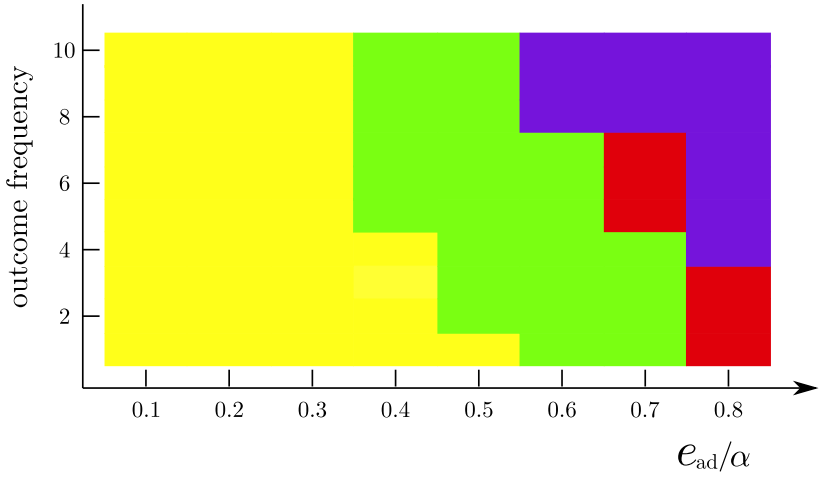


Figure S11. Cumulative histogram of final configurations as a function of the adhesion strength for a domain with $r_{domain} = 35\sigma$ and $\gamma = 1.9k_BT/\sigma$. The color code represents the outcome type and follows the same format as in Fig. 4 of the main text: succesful assemby (green), budding of a partial capsid (yellow), stalled assemby with wrapping (red) and malformed assembly (violet).

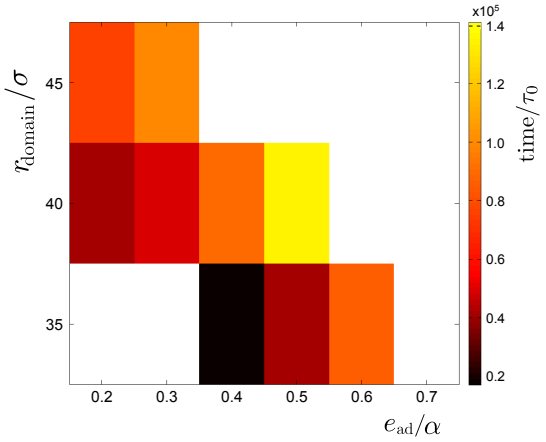


Figure S12. Assembly times. The average time needed for an initial assemblage of three capsomers to complete assembly is shown as a function of the domain radius $r_{\mathrm{domain}}$ and the adhesion energy $e_{\mathrm{ad}}$ for $\gamma = 1.9k_{\mathrm{B}}T/\sigma$. Grid points shown in white indicate parameter values for which assembly was not completed. As noted in the main text, the timescales from these coarse-grained simulations are qualitative.

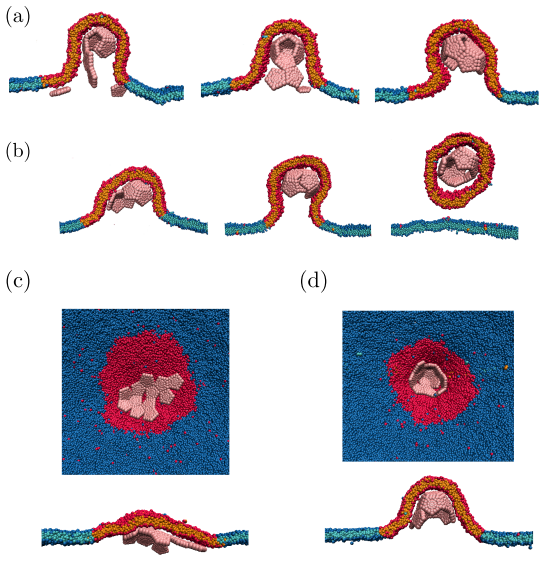


Figure S13. **Kinetic traps.** Simulation snapshots illustrating some typical kinetic traps, for $r_{\mathrm{domain}}$=35$\sigma$ and $\gamma$=1.9$k_{\mathrm{B}}T/\sigma$ with varying $e_{\mathrm{ad}}$ and time steps between subunit injections $\tau_{\mathrm{inject}}$. **(a)** Slices of configurations at different times for $e_{\mathrm{ad}}$=0.5$\alpha$ and $\tau_{\mathrm{inject}} = 1500\tau_0$. A dimer associates with a strained geometry to the growing capsid; therefore, the next subunit is prevented from proper association and a malformed capsid arises. **(b)** Two partial capsids nucleate and then coalesce into a malformed assemblage, which then drives budding of the entire domain. Parameters are $e_{\mathrm{ad}}$=0.3$\alpha$ and $\tau_{\mathrm{inject}}$=0$\tau_0$. **(c)** High values for the adhesion strength $e_{\mathrm{ad}}$=0.6$\alpha$ and injection rate $\tau_{\mathrm{inject}}$=0$\tau_0$ lead to formation of a flat aggregate on the membrane. **(d)** An intermediate adhesion strength $e_{\mathrm{ad}}$=0.5$\alpha$ and high injection rate $\tau_{\mathrm{inject}}$=0 lead to formation of a partial capsid trapped within a flat aggregate. Both top and side views are shown for (c) and (d).

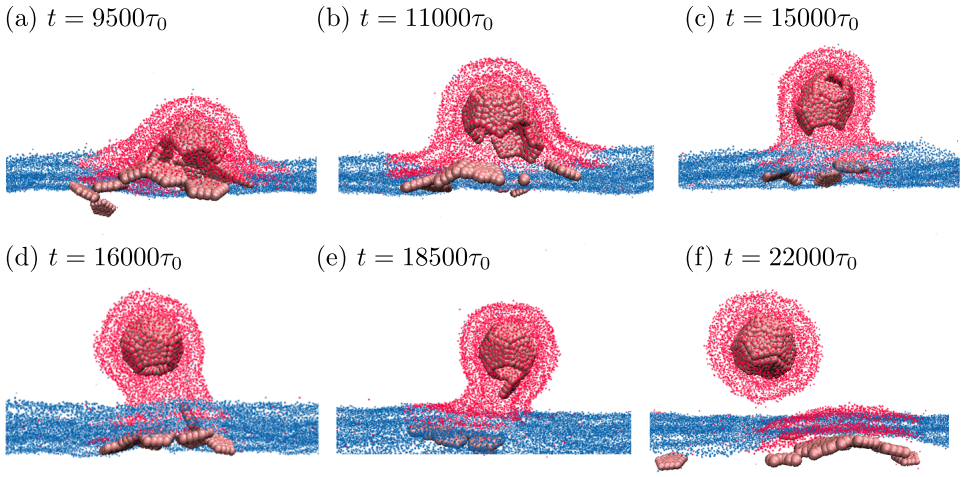


Figure S14. Assembly and budding of a complete capsid in a system with 19 capsomers for $e_{\mathrm{ad}}$=0.3$\alpha$ and $\tau_{\mathrm{inject}}$=500$\tau_0$, $\gamma$=1.9$k_{\mathrm{B}}T/\sigma$, and $r_{\mathrm{domain}}$=35$\sigma$. Side views of the process are shown, with indicated times since the simulation started ($t = 0$). **(a)** When the last subunit is injected ($t$=9500$\tau_0$), the capsid is already half formed. **(b)** Two partial aggregates are formed, and **(c)** assemble into a malformed capsid. **(d)** The capsomers rearrange into an almost finished capsid. **(e)** The last subunit assembles and **(f)** the capsid buds

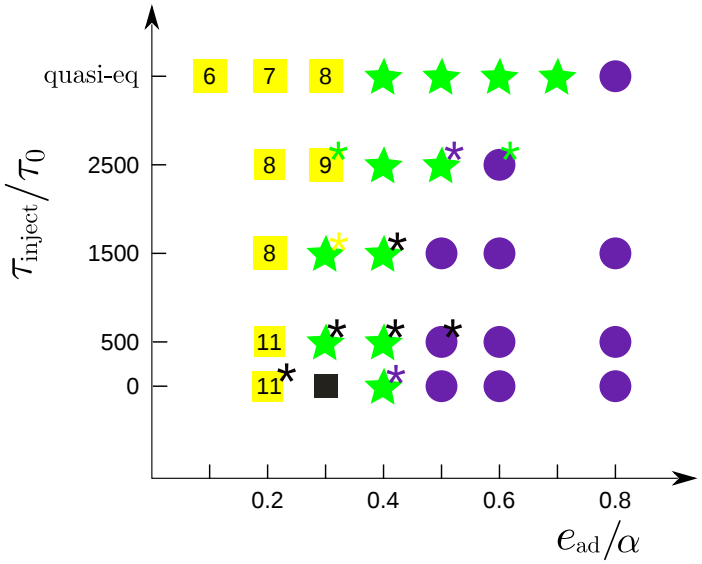


Figure S15. Predominant end products as a function of the subunit injection rate and the adhesion strength for a domain with $r_{\mathrm{domain}} = 35\sigma$ and $\gamma = 1.9k_{\mathrm{B}}T/\sigma$. The most frequent outcome is shown for every set of parameters (with symbols as defined in Fig. 4 of the main text). The asterisks indicate that other behaviors are observed in some trajectories, with the asterisk color representing the nature of the alternative outcomes. Yellow asterisks indicate that some trajectories resulted in incomplete assembly with budding of the entire domain, green asterisks indicate that some trajectories resulted in complete assembly and wrapping, and black asterisks indicate that the alternative behavior is the budding of the whole raft with a malformed capsid as shown in Fig S13b.

Figure S16. The attached movie files show an animation from an assembly trajectory for $e_{\mathrm{ad}}$=0.4$\alpha$, $r_{\mathrm{domain}} = 35\sigma$ and $\gamma = 1.3k_{\mathrm{B}}T/\sigma$. Video S13a shows the beginning of the trajectory, and Video S13b shows the end.

## SUPORTING REFERENCES


[1] Cooke, I., K. Kremer, and M. Deserno, 2005. Tunable generic model for fluid bilayer membranes. *Phys. Rev. E* 72. http://pre.aps.org/abstract/PRE/v72/i1/e011506.

[2] Weeks, J. D., D. Chandler, and H. C. Andersen, 1971. Role of Repulsive Forces in Determining the Equilibrium Structure of Simple Liquids. *J. Chem. Phys.* 54:5237. http://link.aip.org/link/?JCPSA6/54/5237/1.

[3] Grest, G., and K. Kremer, 1986. Molecular dynamics simulation for polymers in the presence of a heat bath. *Phys. Rev. A* 33:3628–3631. http://pra.aps.org/abstract/PRA/v33/i5/p3628_1.

[4] Lipowsky, R., 1993. Domain-induced budding of fluid membranes. *Biophys. J.* 64:1133–1138. http://dx.doi.org/10.1016/S0006-3495(93)81479-6.

[5] Reynwar, B. J., and M. Deserno, 2008. Membrane composition-mediated protein-protein interactions. *Biointerphases* 3:FA117. http://scitation.aip.org/content/avs/journal/bip/3/2/10.1116/1.2977492.

[6] Wales, D. J., 2005. The energy landscape as a unifying theme in molecular science. *Phil. Trans. R. Soc. A* 363:357–375.

[7] Bereau, T., Z.-J. Wang, and M. Deserno, 2014. More than the sum of its parts: Coarse-grained peptide-lipid interactions from a simple cross-parametrization. *J. Chem. Phys.* 140. <GotoISI>://WOS:000334168400042, times Cited: 0 0.

[8] Cooke, I. R., and M. Deserno, 2005. Solvent-free model for self-assembling fluid bilayer membranes: Stabilization of the fluid phase based on broad attractive tail potentials. *J. Chem. Phys.* 123:224710.

[9] Johnston, I. G., A. A. Louis, and J. P. K. Doye, 2010. Modelling the self-assembly of virus capsids. *J. Phys.: Condens. Matter* 22.

[10] Fejer, S. N., T. R. James, J. Hernandez-Rojas, and D. J. Wales, 2009. Energy landscapes for shells assembled from pentagonal and hexagonal pyramids. *Phys. Chem. Chem. Phys.* 11:2098–2104.

[11] Anderson, J. A., C. D. Lorenz, and A. Travesset, 2008. General purpose molecular dynamics simulations fully implemented on graphics processing units. *J. Comput. Phys.* 227:5342–5359. http://dx.doi.org/10.1016/j.jcp.2008.01.047.

[12] Nguyen, T. D., C. L. Phillips, J. a. Anderson, and S. C. Glotzer, 2011. Rigid body constraints realized in massively-parallel molecular dynamics on graphics processing units. *Comput. Phys. Commun.* 182:2307–2313. http://linkinghub.elsevier.com/retrieve/pii/S0010465511002153.

[13] Deserno, M., and W. M. Gelbart, 2002. Adhesion and Wrapping in Colloid-Vesicle Complexes. *J. Phys. Chem. B* 106:5543–5552. http://dx.doi.org/10.1021/jp0138476.